J. Fluid Mech. (2013), *vol.* 724, *pp.* 607–641. © Cambridge University Press 2013
doi:10.1017/jfm.2013.165

Pattern prediction by linear analysis of turbulent flow with drag reduction by wall oscillation

Olivier Blesbois†, Sergei I. Chernyshenko, Emile Touber and Michael A. Leschziner

Department of Aeronautics, Imperial College London, South Kensington Campus, London SW7 2AZ, UK

(Received 1 May 2012; revised 27 February 2013; accepted 20 March 2013; first published online 8 May 2013)

A turbulent flow past a transverse-oscillating wall is considered. The oscillation parameters correspond to the regime where drag reduction is observed. Streak spacing and streak angle obtained from the generalized optimal perturbation approach are compared with results from direct numerical simulations. Other flow features of the generalized optimal perturbation are compared with conditionally-averaged data extracted from numerical simulations. The generalized optimal perturbation at a given instant in time is found to consist of an infinitely long structure at a certain angle to the main flow direction. This angle varies slowly with time for half a period, and then suddenly jumps to a different value, changing both sign and magnitude. The angle variation is shown to be slow, because there is a short time interval in the oscillation period when a small perturbation of a certain angle grows strongly and then remains dominant for almost the entire half-period. The transient growth mechanism of the generalized optimal perturbation is found to be a combination of the Orr mechanism due to the cross-flow shear, acting at the initial stage, followed by the lift-up mechanism of the velocity component directed along the structure by the wall-normal motion also oriented in the same direction.

Key words: boundary layer structure, drag reduction, turbulent flows

1. Introduction

Turbulence is dominated by strongly nonlinear interactions. In contrast, linearized equations are generally assumed to give useful information about a nonlinear system when the nonlinear terms are small. However, *this is not the only case when a linearized approach can be justified.* Consider, for example, a nonlinear device containing a linear filter and a number of nonlinear elements. Suppose that in this system there are broadband fluctuations. Suppose also that the filter is a narrow-pass filter. Then, while at the input of the filter the signal is broadband, the output of the filter will be a narrow-band signal; it will have a dominant frequency. One can disassemble the device, take the filter into the laboratory, and study it there, separately. As a result of this linear analysis (the filter itself is linear, and no nonlinear components were brought into the laboratory) one can determine the band-pass properties and, hence, will be able to predict the dominant frequency at the output

† Email address for correspondence: olivier.blesbois08@imperial.ac.uk

https://doi.org/10.1017/jfm.2013.165 Published online by Cambridge University Press

of the filter when it works as a part of the nonlinear system. For this only a linear analysis is required, and the nonlinear effects in the full system need not be small.

Linearized equations provide useful information about nonlinear turbulence in spite of the nonlinear terms not being small, because for some features of a developed turbulent flow, the selective properties of the linearized Navier–Stokes operator are stronger than the selective properties of the nonlinear terms. This fact explains the existence and properties of certain organized structures observed in turbulent flows. Lee, Kim & Moin (1990), on the basis of numerical simulations motivated by rapid distortion theory, noted that 'the dominant mechanism in the production (and maintenance) of the preferred structures (i.e. streaks) in all turbulent shear flows at high shear rate is a selective amplification of eddies primarily by the linear interaction with mean shear'. In the present paper, the idea of filtering in its particular form described by Chernyshenko & Baig (2005) is applied to analysing the time-dependent pattern of the turbulent flow past a spanwise-oscillating wall at conditions at which drag reduction is observed.

We reiterate that in the present context the idea of filtering means a statement that in a developed turbulent flow the selective properties of the linearized Navier–Stokes operator are stronger than the selective properties of the nonlinear terms, and that this fact explains the existence and properties of certain organized structures observed in turbulent flows.

1.1. *Turbulent drag reduction by spanwise oscillations*

The ability of spanwise wall oscillations to reduce the skin friction in turbulent flow was first demonstrated numerically by Jung, Mangiavacchi & Akhavan (1992), following earlier experimental and numerical observations of transient drag reduction due to imposed spanwise shear made by Bradshaw & Pontikos (1985) and Moin *et al.* (1990). An experimental verification was obtained soon (Laadhari, Skandaji & Morel 1994). This prompted numerous investigations, resulting in significant progress. In particular, it was demonstrated numerically that the overall power balance can also be positive (Baron & Quadrio 1996). Choi & Clayton (2001) found that the near-wall burst activity is decreased when the wall oscillates. Within a certain range of situations, the drag reduction level achieved by spanwise oscillations was demonstrated (Quadrio & Ricco 2004) to collapse as a function of an empirical parameter proposed by Choi (2002), usually denoted S^+, which combines the oscillation period, its amplitude, the penetration depth of the Stokes layer, and the spanwise acceleration at a certain distance from the wall, all scaled with wall units. Wall units are non-dimensional units based on the mean skin friction τ, kinematic viscosity ν, and density ρ. Quantities in wall units are usually marked with a superscript '+'. It was also shown that the drag reduction decreases as the Reynolds number increases (Ricco & Quadrio 2008; Touber & Leschziner 2012). Quadrio, Ricco & Viotti (2009) investigated a more complicated form of the in-plane wall motion where the spanwise velocity has the form of a travelling wave $w_w = A\sin(k_x x - \omega t)$, where x is the coordinate in the mean flow direction. Calculations over a range of the wavenumbers k_x and frequency ω revealed a rich behaviour with regions of both drag reduction and drag increase. The maximum drag reduction and net power saving achieved in channel flow at $Re_\tau = 200$ were 48 % and 18 % respectively. Such high values are quite encouraging.

Despite many past studies, the precise mechanism of drag reduction by spanwise oscillation is not entirely clear, although recent direct numerical simulation (DNS) studies by Touber & Leschziner (2012) have provided new insight into the interaction between the rate of change of the near-wall strain and streak properties. Many

https://doi.org/10.1017/jfm.2013.165 Published online by Cambridge University Press

authors suggested that spanwise oscillations disrupt the turbulence regeneration cycle (Karniadakis & Choi 2003), but no quantitative prediction has been made to underpin this idea. Kim & Lim (2000) showed numerically that removing the linear part of the coupling term between the longitudinal and wall-normal velocity in the Navier–Stokes equation suppresses turbulence, thus indicating that linear effects can be linked to drag. Using only linearized Navier–Stokes equations Duque-Daza *et al.* (2012) demonstrated that the complicated dependence of drag reduction on k_x and ω is very similar to the behaviour of the magnitude of the transient growth of a certain initial disturbance. Moarref & Jovanović (2012) used the linearized equations to predict quantitatively the effect of spanwise wall oscillations on the drag. The findings of Duque-Daza *et al.* (2012) and Moarref & Jovanović (2012) indicate that a linear mechanism is involved in drag reduction and might provide a practical tool for optimizing open-loop control schemes. Since the present paper is concerned with the flow patterns in the drag-reduction regime, rather than with the drag reduction per se, readers interested in the latter are referred to the reviews of Karniadakis & Choi (2003) and Quadrio (2011), and to the latest works cited above. It remains to note that it is generally believed that the mechanism of drag reduction is related to the organized structures observed in near-wall turbulent flows, streaks in particular. This is the main motivation for the present study.

1.2. *Near-wall streaks*

The existence of streaks, that is coherent elongated regions where the instantaneous velocity is below its mean value, has been known for many years (Kline *et al.* 1967). Robinson (1991) gives a comprehensive review of studies on coherent structures in turbulent flows published before 1990. A collection of later work can be found in Panton (1997). Streaks are often visualized in planes parallel to the wall. The streak spacing (distance between the centres of neighbouring streaks) depends on the distance from the wall to the plane in which the measurement is done (Smith & Metzler 1983). Close to the wall the average streak spacing is about 100 wall units, the most probable streak spacing is about 80 wall units, and the streak length is about 1000 wall units. As the visualization plane is moved away from the wall, the streak spacing increases significantly. Further away from the wall, there are super-streaks, of much larger size, and their influence on the near-wall region is not negligible, although it may well be that it amounts only to a quasi-steady modulation of the near-wall turbulence (Chernyshenko, Marusic & Mathis 2012). While the self-sustaining turbulence mechanism can be influenced by these outer-layer structures, it does not require them to exist (Jiménez & Moin 1991). The reader is referred to one of the latest papers, by Hutchins *et al.* (2011), for further details on the large structures. Close to the wall, below approximately 50 wall units, streak parameters expressed in wall units are independent of the Reynolds number. We shall limit further discussion to this near-wall region. Other structures, in particular vortices situated in the buffer layer between $y^+ = 20$ and $y^+ = 50$ (Kim, Moin & Moser 1987), might also be observed near the wall, but in the present study attention will be devoted primarily to streaks.

There is a general agreement about the role of the lift-up mechanism in the formation of streaks: areas of smaller velocity appear because there are wall-normal motions transporting slow-moving near-wall fluid away from the wall. However, explaining why this process leads to the presence of a relatively regular pattern turns out to be much more complicated. The most natural idea is that areas of smaller velocity have a pattern because the wall-normal motions creating these areas have a pattern. A large variety of patterns of wall-normal motion has been suggested,

https://doi.org/10.1017/jfm.2013.165 Published online by Cambridge University Press

including longitudinal vortices, hairpin vortices, and hairpin packets (Adrian 2007). Consequently, the pattern of wall-normal motions has to be explained, and this naturally leads to the idea of a cycle of pattern regeneration, with vortices generating streaks and streaks generating vortices, possibly with some additional structures (for example oblique waves) also involved in the cycle. It is also natural to associate this pattern regeneration cycle with the turbulence energy regeneration cycle necessary for turbulence to sustain itself (Hamilton, Kim & Waleffe 1995; Waleffe 1998; Jiménez & Pinelli 1999; Schoppa & Hussain 2002).

Many approaches to predicting the near-wall regeneration cycle exist. One of them rests on travelling wave solutions (Kawahara & Kida 2001; Waleffe 2001; Faisst & Eckhardt 2003; Kerwell & Tutty 2007; Kawahara 2009), or relative periodic orbits (Viswanath 2007; Duguet, Pringle & Kerswell 2008; Kerwell & Tutty 2007). Relative periodic orbits are solutions to the Navier–Stokes equation that are time periodic in a frame of reference moving with a suitable speed. There are reasons to believe (Cvitanović & Gibson 2010) that with a sufficient number of travelling waves and periodic orbits, the fidelity of the representation of the turbulent flow they provide can be high. The approach of calculating a large number of relative periodic orbits remains, however, prohibitively expensive from the computational viewpoint. The idea of filtering is complementary to the relative periodic orbit concept. Overall, the mechanism of streak formation in near-wall turbulent flows remains an area of continuing research.

A review of the effects of transverse motion on the structure of near-wall turbulence is given by Karniadakis & Choi (2003). In the flow past a spanwise-oscillating wall, streaks become oblique – that is in a wall-parallel plane they are elongated in a direction at a non-zero angle to the mean flow. The streak angle varies with time. The streak strength varies strongly with time, so that during certain time intervals the streaks are difficult to identify. The near-wall streaky structure is also affected by the large-scale motions in the outer part of the flow (Touber & Leschziner 2012), but this effect is outside the scope of the present study. Choi, Clayton & Debisschop (1998) explain the streak-angle variation by the advection of the streaks associated with the spanwise motion (from the viewpoint of streaky pattern being dictated by the pattern of vortices, although their explanation can equally be applied to the streaks). Their explanation corresponds to the situation when the oscillating wall is adjacent to a non-oscillating section upstream. When streaks (or vortices that create the streaks within the streak formation mechanisms they presume) approach the oscillating wall section, the downstream ends of the streaks are moved sideways in the direction of the wall motion, turning the streak (or the vortex). This mechanism does work near the leading edge of the oscillating section of the wall, as can clearly be seen from the figures included in their paper. However, further downstream the angle actually observed has a sign opposite to that of the angle predicted by this mechanism (Touber & Leschziner 2012).

Ricco (2004) suggested a different mechanism, pointing out that typical streaks are inclined in the wall-normal direction, so that their downstream end is further away from the wall than the upstream end. Since the spanwise velocity induced by the oscillating wall decreases with the distance from the wall, the amplitude of the oscillations of the upstream end of the streak is greater than that of the downstream end. This explanation gives the streak angle of the same sign as that observed in reality. However, both in numerical and physical experiments, the streak-angle variation is usually identified by visualizing streaks in a plane parallel to the wall, where the spanwise velocity induced by wall oscillations is the same near the upstream

https://doi.org/10.1017/jfm.2013.165 Published online by Cambridge University Press

and downstream end of the streak, so that the proposed mechanism should not work; yet, streak-angle variation is observed. To overcome this difficulty, one could try to complement this mechanism with viscosity effects leading to the velocity diffusion in the wall-normal direction. In any case, so far none of the above mechanisms has been used to make quantitative predictions of the streak angle. Such predictions are made in § 4.5 of the present paper, and the mechanisms are discussed in § 5.4.

1.3. *Linear approaches in the theory of developed turbulence*

The application of linearized equations to turbulent flows has a long history. It is of particular interest here to discuss the motivation for such studies, because each particular justification of the use of linearized equations determines how they should be used, and how the results should be interpreted.

One has to distinguish between small organized disturbances introduced externally into a turbulent flow, as in Reynolds & Hussain (1972), Gaster, Kit & Wygnanski (1985), Sen & Veeravalli (1998) and Sen *et al.* (2007), and the organized motions intrinsically present in a developed turbulent flow, which are the object of the present study.

The simplest justification for the use of linearized equations rests on the assumption that the nonlinear terms are small. This is the case in the rapid distortion theory (RDT) (Batchelor & Proudman 1954; Hunt 1973; Hunt & Kevlahan 1993; Cambon & Scott 1999), where statistically-stationary turbulence is decomposed into a mean velocity and a fluctuation, and the nonlinear terms in fluctuation velocity are treated as forcing and considered to be small. In particular, Lee *et al.* (1990) refer to RDT as the theory explaining streak formation. Landahl (1975) assumes that strong nonlinearity is localized in space and time, thus justifying the use of linearized equations outside the localized regions. In developed turbulent flows, however, the nonlinear effects are not always small and seldom localized.

Another possible justification for the use of linearized equations in developed turbulence follows from the observation that in many situations, for example in the case of a fluid layer heated from below, the patterns observed in nonlinearly-saturated systems are close, qualitatively and sometimes quantitatively, to the patterns of the fastest-growing linear instabilities. While the general reasons for this behaviour might not be fully understood, one can simply use this justification instead of assuming that the nonlinear terms are small. However, the patterns observed in developed turbulence are quite different from the pattern of the most unstable modes of the corresponding laminar flow. An obvious modification of the instability analysis is to consider linearization about the mean turbulent velocity rather than about the laminar velocity. Since such a base flow is stable, transient growth analysis has to be used. This approach was applied with a certain degree of success in Butler & Farrell (1993) and, with the use of an eddy viscosity, in Del Álamo & Jiménez (2006), Pujals *et al.* (2009), and Cossu, Pujals & Depardon (2009). However, Butler & Farrell (1993) had to introduce strong additional assumptions in order to obtain an agreement with experiments. With the eddy viscosity, the optimal energy growth was found to have two peaks in the spanwise wavelength, one scaling in outer units, supposedly corresponding to large-scale structures, and a secondary peak scaling in inner units, supposedly corresponding to near-wall streaks spaced at about 100 wall units. The question of the use of the eddy viscosity in predicting organized structures is discussed in the next section.

Yet another way of using linearized equations is to treat the nonlinear terms as a form of stochastic forcing. This idea stems from the work on RDT (Batchelor &

https://doi.org/10.1017/jfm.2013.165 Published online by Cambridge University Press

Proudman 1954) and the work of Landahl (1975), and was developed in a number of subsequent studies, only a fraction of which can be cited here (Farrell & Ioannou 1993*b*; Nazarenko, Kevlahan & Dubrulle 2000; Bamieh & Dahleh 2001; Jovanović & Bamieh 2001, 2005; Hwang & Cossu 2010; Jovanović & Georgiou 2010). In fact, the stochastic forcing and the transient growth analysis are related and are sometimes combined successfully (McKeon & Sharma 2010). Naturally, the properties of the solution of the linearized equations with stochastic forcing depend on the properties of the forcing. Various assumptions were made about the properties of the forcing in some of these studies, while others focused on input–output analysis of the linearized Navier–Stokes equations in general.

Chernyshenko & Baig (2005) argued that only those properties of the solutions of the linearized equations with broadband forcing that are due to the selectivity of the linearized Navier–Stokes operator can be meaningfully compared with turbulent flow. Systematically applying this idea to the transient growth analysis approach they concluded that the norm used to measure the magnitude of the perturbation should be directly linked to the flow property that is to be predicted. By way of extensive comparisons they confirmed that adherence to this rule significantly improves the quality of the predictions. Lockerby, Carpenter & Davies (2005) and Carpenter *et al.* (2007) also calculated perturbations that maximized not the entire energy of the perturbation, but different measures of its magnitude, and obtained agreement with the results of various numerical and physical experiments.

2. Methodology: generalized optimal perturbation approach

2.1. *The main ideas*

The velocity $\boldsymbol{u}$ of a developed incompressible turbulent flow can be represented as $\boldsymbol{u} = \boldsymbol{U} + \boldsymbol{u}'$, the sum of a base flow $\boldsymbol{U}$ and a fluctuation $\boldsymbol{u}'$. One can then rewrite the full Navier–Stokes equations with the fluctuations as new variables, placing the linear terms on the left-hand side and the nonlinear terms on the right-hand side:

$$\frac{\partial \boldsymbol{u}'}{\partial t} + \boldsymbol{U}\cdot\nabla\boldsymbol{u}' + \boldsymbol{u}'\cdot\nabla\boldsymbol{U} + \nabla p - \frac{1}{Re}\Delta\boldsymbol{u}' = \boldsymbol{F}, \tag{2.1}$$

$$\boldsymbol{F} = -\frac{\partial \boldsymbol{U}}{\partial t} - \boldsymbol{U}\cdot\nabla\boldsymbol{U} - \boldsymbol{u}'\cdot\nabla\boldsymbol{u}' - \nabla P + \frac{1}{Re}\Delta\boldsymbol{U}. \tag{2.2}$$

The base flow $\boldsymbol{U}$ is assumed incompressible and satisfying the same boundary conditions as $\boldsymbol{u}$, so that the fluctuation velocity $\boldsymbol{u}'$ satisfies homogeneous boundary conditions and the continuity condition:

$$\nabla\cdot\boldsymbol{u} = 0, \quad \nabla\cdot\boldsymbol{u}' = 0. \tag{2.3}$$

In this paper, $\boldsymbol{u}'$ is referred to as a fluctuation velocity when it corresponds to a real turbulent flow field, and as a perturbation velocity when it is used in the linearized Navier–Stokes equation framework.

In several studies involving optimal perturbation approach for uncontrolled (Del Álamo & Jiménez 2006; Cossu *et al.* 2009; Pujals *et al.* 2009) and controlled (Moarref & Jovanović 2012) flows, the use of turbulent viscosity gave interesting and important results (note that the turbulent viscosity of the controlled flow was computed in the later paper using stochastically forced linearized dynamics). The now classical approach to introducing turbulent viscosity into the analysis of organized structures stems from the work of Reynolds & Hussain (1972), who introduced a triple decomposition $\boldsymbol{u} = \bar{\boldsymbol{u}} + \tilde{\boldsymbol{u}} + \boldsymbol{u}''$, where $\bar{\boldsymbol{u}}$ is the mean (time-averaged) field, $\tilde{\boldsymbol{u}}$

https://doi.org/10.1017/jfm.2013.165 Published online by Cambridge University Press

is the organized part of the motion, and $\boldsymbol{u}''$ corresponds to the disorganized part. In Reynolds & Hussain (1972), as well as in the recent works of Sen & Veeravalli (1998, 2000) the organized part was defined using phase-averaging. This corresponds to the situation when the organized disturbances are introduced externally into the turbulent flow, for example by periodic suction and blowing through the wall, as in Sen *et al.* (2007). In contrast, in the present paper organized structures inherently present in the flow are studied. In the case of Reynolds & Hussain (1972) both time-averaging and phase-averaging smooths streaks out, so that streaks are included in $\boldsymbol{u}''$ and not predicted as part of the organized component $\tilde{\boldsymbol{u}}$. However, if streaks are to be predicted as part of the solution of the equations for $\tilde{\boldsymbol{u}}$ then $\boldsymbol{u}''$ does not contain streaks. Since the Reynolds stresses are mostly produced by streaks, in the case when $\boldsymbol{u}''$ does not contain streaks $\langle \boldsymbol{u}''\boldsymbol{u}'' \rangle$ is considerably smaller, and the corresponding turbulent viscosity must also be smaller than it is in the case when the Reynolds stress is generated by the entire fluctuating field including streaks. In any event, Reynolds stresses are small near the wall. For this reason a laminar viscosity is used in the present study.

Equation (2.1) defines a linear operator that gives $\boldsymbol{u}'$ if applied to $\boldsymbol{F}$. The generalized optimal perturbation (GOP) approach (Chernyshenko & Baig 2005) evolved from the empirical observation that this linearized Navier–Stokes operator acts as a band-pass filter for the longitudinal velocity as a function of the spanwise coordinate, and as a low-pass filter with respect to the longitudinal coordinate, so that certain properties of $\boldsymbol{u}'$ are determined by the filtering properties of the left-hand side of (2.1) to a much greater degree than by the precise form of $\boldsymbol{F}$. As the result of this property, when the right-hand side is broadband (that is when the characteristic width of the spectrum of the input is noticeably greater than the passband width of the filter), the output of this filter has a streaky pattern. In this case the streak spacing is determined mostly by the wavenumber around which the passband of the filter is centred, and the streak spacing can be approximately found by analysing the linearized system only. This does not require the fluctuations to be small. In the present study, the GOP approach is used to obtain qualitative insight into the pattern-formation mechanisms in a turbulent flow past a spanwise-oscillating wall. This section outlines the basics of the approach and its adaptation to the case of turbulent flows with spanwise wall oscillations.

The filtering properties of the linearized Navier–Stokes operator can be investigated by various means. One way is to extract the linearized Navier–Stokes operator from the system (2.1) and (2.2) and investigate it in isolation; for example, by considering its response to different test inputs. In order to find the centre of the passband, one can maximize the magnitude of the output over all possible inputs of unit magnitude. Obviously, the maximum will be attained at such an input that is inside the passband, thus indicating the passband location in the spectrum. This is the idea of using optimal perturbations in the present context.

The choice of the base flow affects both the properties of the linearized system on the left-hand side of (2.1) and the properties of $\boldsymbol{F}$. Intuitively, one can suggest a choice of $\boldsymbol{U}$ in such a way as to minimize the nonlinearity represented by $\langle \boldsymbol{u}'^2 \rangle$, where $\langle \cdot \rangle$ denotes ensemble-averaging. Since $\langle \boldsymbol{u}'^2 \rangle = \langle (\boldsymbol{u} - \boldsymbol{U})^2 \rangle = \langle (\boldsymbol{u} - \langle \boldsymbol{u} \rangle)^2 \rangle + (\langle \boldsymbol{u} \rangle - \boldsymbol{U})^2$, it is minimized when $\boldsymbol{U} = \langle \boldsymbol{u} \rangle$. In the case of a periodic oscillation of the wall, it is reasonable to select the statistical ensemble in such a way that the phase information is preserved, so that $\langle \cdot \rangle$ denotes phase-averaging. Then $\boldsymbol{U}$ will be a periodic function of time. The above arguments are only intuitive: instead, one could simply assume that taking the base flow to coincide with the mean (or phase-averaged) flow is part of the empirical observation of the filtering property on which the GOP approach is based.

https://doi.org/10.1017/jfm.2013.165 Published online by Cambridge University Press

The simple filter analogy implies that the output of the filter is a real-valued function of one variable. However, the output of the linearized Navier–Stokes operator is a vector function of time and three spatial variables. Therefore, before one can use the filter analogy, the output of the linearized Navier–Stokes operator has to be reduced to a function of a single variable. It is important that the filtering properties – for example, the wavelength at the centre of the passband – vary strongly depending on the nature of this reduction. In Chernyshenko & Baig (2005) the reduction was achieved by considering the longitudinal velocity component at a fixed distance from the wall. As a result, the streak spacing was obtained as a function of the distance from the wall, thus allowing comparison over a wide range of parameters. Technically, this selection was made by using a special norm of the output, different from the norm used for the input, while studying the properties of the filter by solving the optimal perturbation problem. Hence, this approach is a generalization of the standard optimal perturbation theory. Since the same technique is used in the present study, it will be discussed in more detail below, but the general idea of the filter properties being strongly dependent on the choice of what is considered to be the filter output is emphasized here and is essential to understanding the entire approach. Another way of looking at this technique is to consider the linearized Navier–Stokes operator as a collection of different filters sharing the same input $\boldsymbol{F}$ but having separate outputs.

When the filtering properties of the linearized Navier–Stokes operator are studied using optimal perturbations, the solution of the optimization problem is the input of a unit norm that maximizes the norm of the output. The corresponding solution of the linearized Navier–Stokes equations can readily be interpreted as a fluid flow. Another crucial point to appreciate is the nature of the relationship between this flow and the turbulent flow described by (2.1) and (2.2). The idea of a filter explains why one can expect that the output of the filter that is maximized in calculating the optimal perturbation should be similar to the output of the same filter when it is part of the full nonlinear Navier–Stokes system. However, the other parts of the optimal perturbation, whether they can be interpreted as inputs or as outputs of the other filters constituting the linearized Navier–Stokes operator, might differ arbitrarily from the corresponding parts of the turbulent flow. The obvious example is the classical optimal perturbation consisting of longitudinal vortices and streaks. The streaks of the optimal perturbation are the features whose magnitude is maximized over all possible inputs and, therefore, they can be expected to be observed in the turbulent flow as well. The longitudinal vortices of the optimal perturbation are not strong (in fact they usually decay monotonically). Hence, there is no reason to expect that such vortices would be observed in a turbulent flow. This is indeed the case, as visualizations of instantaneous near-wall turbulent flow do reveal long streaks but do not reveal similarly long vortices (Adrian 2007).

However selective the linearized Navier–Stokes operator is, the exact properties of the solution of the full Navier–Stokes system depend also on the exact properties of $\boldsymbol{F}$. When information about the properties of $\boldsymbol{F}$ is limited to $\boldsymbol{F}$ being broadband, there is inevitable loss of accuracy in the prediction. For this reason, the GOP approach is more suitable for analysing the qualitative mechanisms of the developed turbulent flow than for making precise quantitative predictions.

2.2. *Generalized optimal perturbations for time-periodic base flow*

Chernyshenko & Baig (2005) demonstrated that the selectivity properties of the linearized Navier–Stokes operator can be established without excessive loss of accuracy by maximizing the magnitude of the solution over a special form of the

https://doi.org/10.1017/jfm.2013.165 Published online by Cambridge University Press

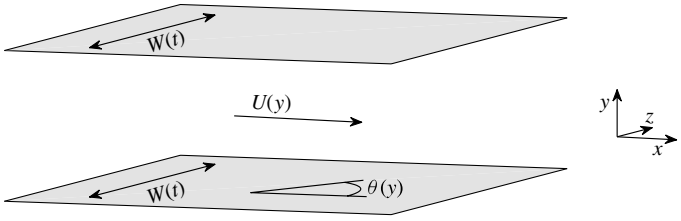


FIGURE 1. Flow configuration. The component $U(y)$ of the mean flow in the streamwise direction x is independent of time. The two walls are moving in phase in the spanwise direction z, and θ is the angle between the streaks and the streamwise direction.

right-hand side, in which the dependence on time is restricted to a Dirac delta function: $\boldsymbol{F} = \boldsymbol{u}_i'(\boldsymbol{x})\delta(t - t_i)$. With this form of forcing, (2.1) reduces to an initial-value problem for the homogeneous linear equation with a given initial condition $\boldsymbol{u}' = \boldsymbol{u}_i'$ at $t = t_i$. The solutions of such an initial value problem can be either diverging or asymptotically stable, presenting potentially important transient growth before converging to zero. The GOP approach applies only if the mean flow is asymptotically stable.

We shall compare the properties of the streaky structures observed in DNS with the GOP predictions. It is implied that a finite computational domain is considered for a flow in a plane channel (figure 1). The streaky structures will be identified by the value of the longitudinal velocity in a given plane parallel to the wall. For the optimal perturbation to describe the corresponding filtering properties of the linearized Navier–Stokes operator, the measure of the magnitude of the solution has to be the magnitude of the longitudinal velocity in the same plane. Accordingly, we will use the following final time norm $\| \ \|_f$:

$$\|\boldsymbol{u}'\|_f^2 = \frac{1}{S}\int_{y=y_0} u^2 \,\mathrm{d}x\,\mathrm{d}z, \tag{2.4}$$

where the streamwise direction is denoted x, the wall-normal direction is y, the spanwise direction is z, the corresponding components of the perturbation-velocity vector are $\boldsymbol{u}' = (u, v, w)$, y_0 is the coordinate of the particular plane in which the comparison with DNS is to be made, and S is the area of the cross-section of the computational domain at $y = y_0$. In other words, the final norm squared equals twice the average of the energy of the longitudinal component of the perturbation at the distance y_0 from the wall. The same norm was used in Chernyshenko & Baig (2005).

The norm measuring the magnitude of the initial perturbation could be used to incorporate the available information on the properties of the right-hand side of (2.1), but since we cannot guess the properties of the actively controlled flow, the simplest norm will be used:

$$\|\boldsymbol{u}'\|_i^2 = \frac{1}{V}\int_V \left(u^2 + v^2 + w^2\right) \,\mathrm{d}x\,\mathrm{d}y\,\mathrm{d}z, \tag{2.5}$$

where V is the volume of the domain. This is similar to one of the norms used by Chernyshenko & Baig (2005), but all three velocity components are included here instead of only v and w, since we cannot expect that the initial condition of the optimal perturbation will have $u = 0$ in the present case.

https://doi.org/10.1017/jfm.2013.165 Published online by Cambridge University Press

The generalized optimal perturbation $\boldsymbol{u}_{gop}(t_f, t, x, y, z)$ is defined as the solution $\boldsymbol{u}'$ of the following optimization problem:

$$A(t_f) = \max_{\boldsymbol{u}'(t_i), t_i < t_f - \varepsilon} \frac{\|\boldsymbol{u}'(t_f)\|_f^2}{\|\boldsymbol{u}'(t_i)\|_i^2}, \tag{2.6}$$

where $\boldsymbol{u}'(t)$ satisfies the homogeneous ($\boldsymbol{F} = 0$) linearized Navier–Stokes equation (2.1), and $\varepsilon > 0$ is a small suitably selected constant. Optimizing over t_i is appropriate because the solution for a general form of $\boldsymbol{F}$ can be represented as a convolution product of solutions with impulse forcing. The velocity field $\boldsymbol{u}_{gop}$ depends on both the physical time (or phase) t_f at which the comparison with DNS is to be made and its own time variable t, and is the perturbation achieving the largest possible amplification factor A at $t = t_f$.

For $\varepsilon = 0$ the solution of this optimization problem is $t_i = t_f, A = \infty$, and $\boldsymbol{u}'$ is zero everywhere, except the plane $y = y_0$, where it has a non-zero u component. Such a solution is physically meaningless, since it corresponds to the case when $\boldsymbol{F}$ is concentrated in the plane $y = y_0$, and regardless of how little we might know about $\boldsymbol{F}$, such a possibility can be excluded. This issue could be avoided by modifying $\|.\|_i$. However, since the solution with such initial conditions quickly decays, it is technically easier to eliminate it by introducing $\varepsilon > 0$ into the definition. Note that for values of ε such that the optimization procedure gives $t_f - t_{i,opt} > \varepsilon$, where $t_{i,opt}$ is the optimal initial time, the result becomes independent of the particular value of ε. We always select ε so that this is the case.

If the mean flow does not depend on time then $\boldsymbol{u}_{gop}$ does not depend on t_f, and optimizing over t_i with fixed t_f would give the same result as the commonly used optimization over t_f with fixed t_i.

3. Base flow

A flow in a plane channel with oscillating walls is considered. The spanwise velocity of both walls is $W = W_m \cos(2\pi t_f/T)$, where t_f is time, and T is the period of oscillation.

Since drag reduction by wall oscillations is linked to near-wall processes, it is appropriate to measure variables in wall units (Quadrio 2011). Wall units depend on the wall friction. The DNS (Touber & Leschziner 2012), which will form the basis for our comparisons, was conducted at a fixed bulk Reynolds number. Thus, the skin friction in the controlled flow is not known until the numerical simulation has been performed, and the scaled results are not known either. In order to test fully the predictive capabilities of the GOP approach, its input was limited to what is known before the numerical simulation of the controlled flow, even though this might reduce the fidelity of the predictions. Using the channel half-width as the length scale, the longitudinal velocity of the uncontrolled mean flow can be approximated by the Reynolds & Tiederman (1967) formula. With the channel walls placed at ± 1, the streamwise velocity U^+ is obtained by integrating the system:

$$G(y) = \frac{1}{2}\sqrt{1 + \left(0.525\frac{Re_\tau}{3}(1-y^2)(1+2y^2)\left[1 - \exp\left(-(1-|y|)\frac{Re_\tau}{37}\right)\right]\right)^2} - \frac{1}{2}, \tag{3.1}$$

$$\frac{\partial U^+}{\partial y} = \frac{-yRe_\tau}{1+G(y)}. \tag{3.2}$$

https://doi.org/10.1017/jfm.2013.165 Published online by Cambridge University Press

Here, Re_τ is the Reynolds number based on the friction in the uncontrolled flow, that is, the flow with non-oscillating walls. For a case when the plane $y = y_0$ is close to the wall, as it is in the present study, $\boldsymbol{u}_{gop}$ is largely affected by the near-wall part of the velocity profile, which in turn is largely determined by the wall shear. For non-zero wall oscillations, when the drag is reduced, Re_τ is reduced as well, and the near-wall slope of the mean longitudinal velocity profile is also different. In the cases considered in the present study, this difference remained below or about 40 %. It would be interesting to repeat all the calculations for the phase-averaged longitudinal profile obtained from DNS, but from the above considerations it seems plausible that the difference with current results will be of magnitude similar to the error that can be expected from the GOP approach (compare with 30 % margins in figure 8 of Chernyshenko & Baig 2005).

For oscillation period $T^+ \leqslant 200$, the phase-averaged spanwise velocity is known to be very close to that of the laminar Stokes layer (Quadrio *et al.* 2009; Touber & Leschziner 2012). In the GOP simulations, a laminar solution of the Navier–Stokes equation with two walls oscillating in phase was therefore used:

$$W(t_f, y) = C_0 \left\{ \mathrm{e}^{-k(y+1)} \left[\cos(\omega t_f - k(y-1)) + \mathrm{e}^{-2k} \cos(\omega t_f - k(y-1) + 2k) \right] \right.$$
$$\left. + \mathrm{e}^{k(y-1)} \left[\cos(\omega t_f + k(y-1)) + \mathrm{e}^{-2k} \cos(\omega t_f + k(y-1) + 2k) \right] \right\}, \quad (3.3)$$

where $\omega = 2\pi/T$, the oscillation wavenumber $k = \sqrt{\omega/(2\nu)}$, and C_0 is a renormalization constant selected such that at the walls $W(t_f, \pm 1) = W_m \cos(2\pi t_f/T)$.

In this paper, the maximum wall velocity is set to $W_m^+ = 12$, the same as in the DNS used for comparisons.

4. Results and comparisons

4.1. *The basis for the comparisons*

Since the base flow is homogeneous in the spanwise direction, the optimization in (2.6) can be done in two steps. First, the optimization is performed for given spanwise wavenumber and initial time. The second step is an optimization over these two parameters:

$$A_0(t_f, t_i, \lambda_z) = \max_{\boldsymbol{u}'(t_i)} \frac{\|\boldsymbol{u}'(t = t_f)\|_f}{\|\boldsymbol{u}'(t = t_i)\|_i}, \quad (4.1a)$$

$$A(t_f) = \max_{t_i < t_f - \varepsilon, \lambda_z} A_0(t_f, t_i, \lambda_z). \quad (4.1b)$$

Here, λ_z is the spanwise wavelength of the perturbation. More details on the calculation of $A_0(t_f, t_i, \lambda_z)$ are given in the Appendix. The base profile considered in the present work is also homogeneous in the main flow direction, so that the calculations could also be performed separately for each longitudinal wavenumber. This was not done since the code used was developed to solve problems with a mean flow dependent on the streamwise direction. Nevertheless, due to the homogeneity in two directions, the optimal solution can be written in the form $\boldsymbol{u}' = \mathrm{Re}\{\boldsymbol{u}'_{\beta_x,\beta_z}(y,t)\exp[\mathrm{i}(\beta_x x + \beta_z z)]\}$. Since this is invariant with respect to translation in the direction $(1/\beta_x, 1/\beta_z, 0)$, the optimal structure consists of infinitely long oblique streaks.

Examples of the flow patterns observed in DNS are shown in figure 2. The streaks are clearly visible in figure 2(*a*) where $T^+ = 200$, but in figure 2(*b*) where $T^+ = 100$ streaks are less clear and virtually absent from parts of the picture. In general, streaks

https://doi.org/10.1017/jfm.2013.165 Published online by Cambridge University Press

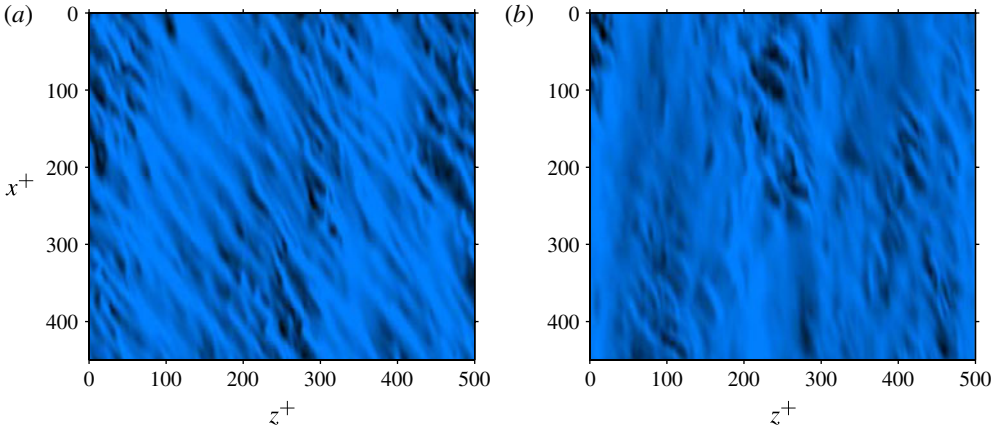


FIGURE 2. (Colour online) Visualization of the streamwise velocity component at a distance $y_0^+ = 11$ from the wall for the friction Reynolds number $Re_\tau = 500$. Snapshot from Touber & Leschziner (2012): (*a*) $T^+ = 200$; (*b*) $T^+ = 100$.

are observed to be less pronounced when the drag reduction is stronger, as is the case of $T^+ = 100$, where the drag reduction is close to the maximum achievable. This can be attributed to streaks having an amplitude comparable to the footprint of the outer large-scale structures when the drag is reduced. Streaks are more evident during certain parts of the oscillation period, and become indistinct over the other parts of the period. When streaks are visible, their angle varies with time, although the variation is not large. The sign of the angle changes during the part of the oscillation period when the streaks are indistinct. More details of the DNS are given in Touber & Leschziner (2012). The complicated behaviour of the streaky pattern makes comparisons difficult, but at the same time allows comparing more features than only the streak spacing.

The majority of the calculations of $\boldsymbol{u}_{gop}$ were performed for the Reynolds number $Re_\tau = 180$, for the non-oscillating case and for oscillating-wall cases with oscillation periods $T^+ = 100$ and $T^+ = 200$, at different distances from the wall and for different observation phases in the period. Some calculations were also performed for $Re_\tau = 500$ to test the dependence of the results on Re_τ. In the case $Re_\tau = 180$ the grid was uniform in the streamwise and wall-normal directions with $(n_x, n_y) = (193, 180)$ nodes, for a channel of width 2 and length 10. In the case $Re_\tau = 500$, the length of the channel was 5, and the grid had $(n_x, n_y) = (513, 200)$ nodes. Where possible, the results were compared to streaks obtained in the DNS of Touber & Leschziner (2012). The simulations were performed at a bulk Reynolds number $Re_b = 9000$, which corresponds to $Re_\tau \approx 500$ for the baseline flow. The oscillating-wall cases with $T^+ = 100$ and $T^+ = 200$, based on the mean profile of the flow past a non-oscillating wall, were calculated for the same Re_b. Throughout this paper, Re_τ, t^+ and y^+ are defined using the skin friction in the flow with non-oscillating wall. If the actual skin friction extracted from the oscillating-wall DNS results were used, the Reynolds number and actuation period would be $Re_{\tau ac} = 420$ and $T_{ac}^+ = 68$ for the case $T^+ = 100$, and $Re_{\tau ac} = 440$ and $T_{ac}^+ = 150$ for the case $T^+ = 200$.

In this paper the GOP results for $Re_\tau = 180$ will be compared to DNS performed at a different Reynolds number. This is not expected to be a problem because the streak characteristics are only weakly dependent on Re_τ, as long as they are expressed in

https://doi.org/10.1017/jfm.2013.165 Published online by Cambridge University Press

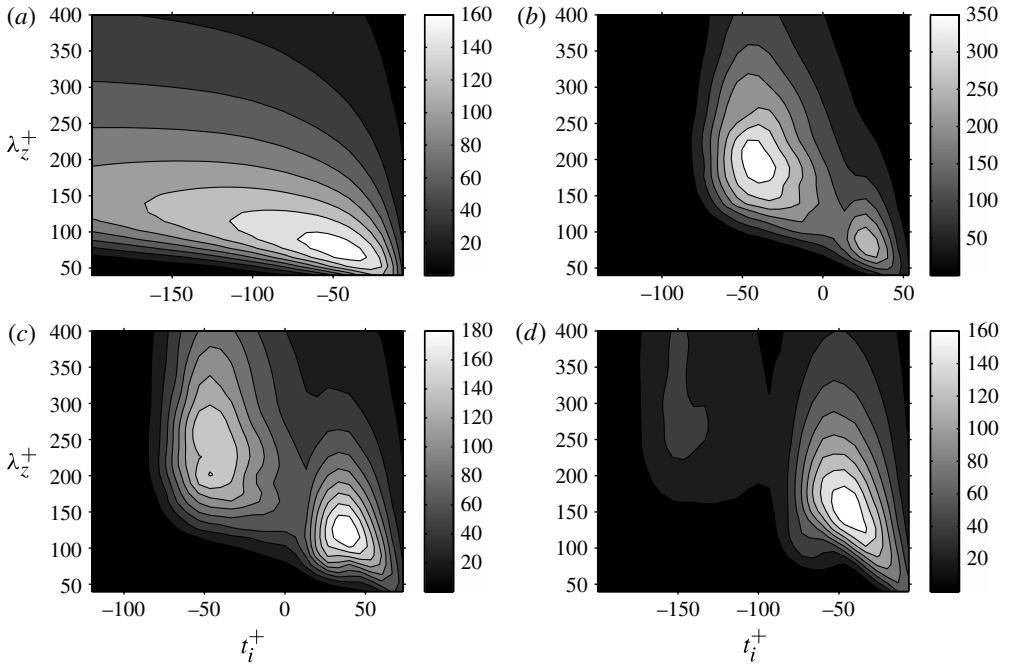


FIGURE 3. Maximum amplification factor $A_0(t_i, \lambda_z, t_f)$: $Re_\tau = 180$, $y_0^+ = 11.25$; and (*a*) non-oscillating wall, (*b*) $t_f^+ = 60$, (*c*) $t_f^+ = 80$, (*d*) $t_f^+ = 0$. The global maximum of each map is $A_0(t_f)$. In the oscillating-wall case the period is $T^+ = 200$, and amplitude of the oscillation is $W_m^+ = 12$.

wall units. This was confirmed in several cases by showing that the GOP results for $Re_\tau = 180$ and $Re_\tau = 500$ were close.

The comparisons of the results in a given plane parallel to the wall amount to the comparison of streak spacing and streak angle of $\boldsymbol{u}_{gop}$ as a function of the oscillation phase and the distance from the wall. Comparisons will also be made between $\boldsymbol{u}_{gop}$ and the conditionally-averaged results of the DNS. It is relevant to point out the symmetry of the wall motion over the two halves of the oscillation period. As a consequence, all results presented in this paper will have the same property, which we will call a 'left–right' symmetry. The streak spacing will be a periodic function with the period equal to half of the forcing period, and if the $\boldsymbol{u}_{gop}$ angle $\theta(t_f, y_0)$ is calculated, then $\theta(t_f + T/2, y_0) = -\theta(t_f, y_0)$.

4.2. *Selectivity of the linearized Navier–Stokes equations for the flow past a spanwise-oscillating wall*

Prior to considering the optimal perturbation for determining the middle point of the passband (see § 2.1), one needs to verify that the idea of a single passband is applicable in the case of the flow past an oscillating wall. Figure 3 shows the energy-amplification factor $A_0(t_i, t_f, \lambda_z)$ for flows past oscillating and non-oscillating walls. The brightest point in each of these pictures represents the GOP amplification factor $A(t_f)$ for the corresponding flow. The temporal window in figure 3 corresponds to one period for the oscillating cases, with spanwise wavelengths up to $\lambda_z^+ = 400$. It is possible, in principle, that the global maximum is located outside this window. In

https://doi.org/10.1017/jfm.2013.165 Published online by Cambridge University Press

order to explore this possibility rigorously one would need to perform a transient-growth analysis based on Floquet theory (see Schmid 2007). Using the present approach, only a few calculations for a longer time (and larger range of λ_z) were made, showing no other maxima and no tendency for perturbation growth outside one period.

In the non-oscillating case (figure 3*a*) the plot would be the same for all t_f. In this case, the energy-amplification factor has one well-defined maximum. This shows that, in this case, $\boldsymbol{u}_{gop}$ has a growth time of about $t^+ = 50$ and a wavelength $\lambda_z^+ = 80$. The corresponding streaky structure is indeed known to dominate the real flow. The situation is quite different for the case of an oscillating wall exemplified by figure 3(*b*). In this case, there are two local maxima, with a relatively small difference in amplitude. This means that a superposition of the two structures corresponding to each of these maxima will be present in the flow. The global maximum at $(\lambda_z^+, t_i^+) \approx (200, -40)$ corresponds to $\boldsymbol{u}_{gop}$, whereas the structure corresponding to the other local maximum is less pronounced, although given its magnitude, it should also contribute to the observed flow pattern. This configuration with two local maxima is observed only over part of the oscillation period, while in the other part of the period, one maximum is much larger than the other. The switch of the global maximum from one local maximum to another is illustrated by figures 3(*b*) and 3(*c*). Therefore, in the real turbulent flow, clear dominant structures can be expected to be present during certain parts of the oscillation period, while in other parts of the period two different structures are competing with each other, making the flow less organized.

4.3. *Drag reduction and flow organization*

There are arguments suggesting that the larger the degree of turbulent flow organization the greater the drag (see, for example, the review by Karniadakis & Choi 2003). Touber & Leschziner (2012) point out 'the virtual absence of small-scale streaks' in the regime with largest drag reduction, while Levich, Handlerand & Sirovich (1993) demonstrate that randomizing the phases of certain modes reduces drag. Hence, it is natural to try to relate the amplification factor of $\boldsymbol{u}_{gop}$ to the drag. One could expect that the amplification factor is smaller when the wall oscillates and the drag is reduced. In fact, while for the case of a non-oscillating wall the energy-amplification factor is 160, for an oscillating wall at $T^+ = 200$, shown in figure 3(*c*) when the drag reduction is substantial, the energy-amplification factor is 400. An explanation of this unexpected result rests on the observation that the width of the A_0 distribution in the t_i direction for the actuated case is much narrower than for the baseline flow. For a non-oscillating wall the most amplified perturbation has amplification factor close to that of $\boldsymbol{u}_{gop}$ over a wide range of t_i, whereas in the case with wall oscillations this range is quite narrow.

An attempt can be made to take into account not only the amplitude but also the width of the peaks, thus considering not only the 'most probable' streaks, but a collection of possible structures contributing to turbulence-energy generation. This was done by integrating the energy A_0 over the available range of (λ_z, t_i), and was also combined with averaging over the observation phase t_f, as only the average drag reduction over a period is relevant. The integral was found to be equal to 6.4×10^4 in the non-oscillating wall case, 5.1×10^4 in the oscillating-wall case at $T^+ = 200$, in which the drag reduction is $\sim$25 %, and 2.5×10^4 for $T^+ = 100$ in which case the drag reduction is $\sim$32 %. This means that the value of the integral does correlate with the drag. Note that the recent works by Duque-Daza *et al.* (2012) and especially Moarref & Jovanović (2012), while not explicitly relating the drag to

https://doi.org/10.1017/jfm.2013.165 Published online by Cambridge University Press

the structural feature of the flow, offer superior (although different) routes to obtaining drag-reduction predictions.

It is difficult to introduce a quantitative measure of organization in a turbulent flow; however, there is a clear difference between the magnitude of fluctuations and the degree of their randomness/organization. The filtering idea suggests that the degree of flow organization can be judged by the relative width of the peaks of the amplification factor. Because the peaks of the amplification factor, shown in figure 3, are narrower (and higher) for flows with reduced drag, by this measure one has to conclude that flows with greater drag reduction are characterized by greater degree of organization. The lack of a visually identifiable structure reported by Touber & Leschziner (2012) for the regime with maximum drag reduction is due to higher complexity of the flow organization, as evidenced by the presence of two peaks in figure 3.

It is relevant to point out here that neither Duque-Daza *et al.* (2012) nor Moarref & Jovanović (2012) link the drag reduction directly to the change in organization of the flow caused by wall oscillations. Duque-Daza *et al.* (2012) considered an initial value problem for linearized Navier–Stokes equations with a certain fixed initial condition. They calculated the evolution of the flow when the base flow is varied due to travelling-wave wall oscillations and demonstrated the correlation between the amplification of this initial condition and the drag when the frequency and the wavenumber of the travelling wave of the wall oscillation are varied. The structure of the flow they calculated differs significantly from the structure of the turbulent flow past an oscillating wall. Moarref & Jovanović (2012) considered a forced response problem with the stochastic forcing having statistical characteristics of the uncontrolled flow. They used the Navier–Stokes equations linearized about the phase-averaged controlled flow, obtained the second-order statistics and calculated the drag by solving the mean velocity equations using a turbulent viscosity that is computed from k and ε, where k and ε are obtained directly from the second-order statistics. This model does not take into account the presence of organized structures, in the sense that both k and ε are isotropic parameters. In terms of simple analogies, the linearized Navier–Stokes equations describe a filter and an amplifier. From the above observations it follows that it is the filtering properties that determine the structure, but that it is the broadband amplification that determines the drag. Hence, it may well be that the drag reduction strategies should aim at reducing the amplification over a range of possible inputs rather than disrupting the flow organization. In the remainder of the paper we will concentrate on flow patterns.

4.4. *Streak spacing*

Comparisons of streak spacing were used by Chernyshenko & Baig (2005) in order to demonstrate the predictive ability of the GOP approach. However, this was only possible because the comparisons were made for a large number (more than 35) of cases resulting in a coverage of a wide range (about an order of magnitude) of streak spacing. Comparisons over such a range can be conclusive even if the nature of the theoretical approach is such that the quantitative error is relatively large, as is the case for the GOP approach. In the case considered in the present study, the variation of streak spacing with various parameters is limited. At the same time, the uncertainties due to the problem of selecting the mean profile without actually performing a DNS (see § 3), the absence of *a priori* information on the distribution of wall-normal stresses, which was used in Chernyshenko & Baig (2005), and the difficulty of determining the actual streak spacing from the DNS results make the

https://doi.org/10.1017/jfm.2013.165 Published online by Cambridge University Press

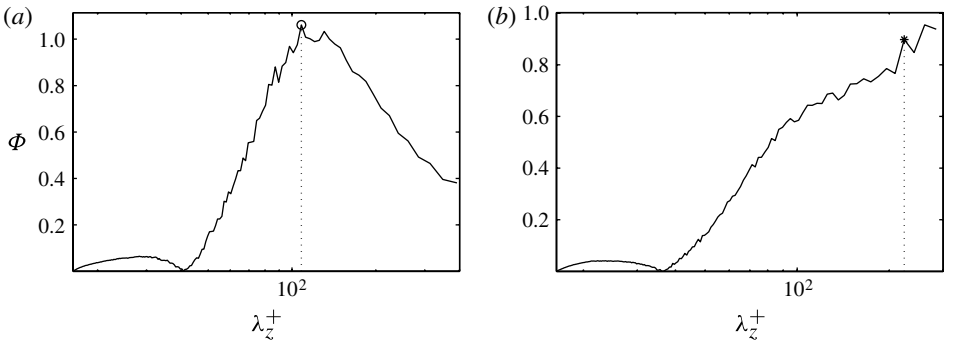


FIGURE 4. Scaled premultiplied DNS spectrum $\Phi = E(\lambda_z)/\lambda_z$ of the streamwise velocity component in two characteristic cases: (*a*) $T^+ = 200, t_f^+ = 40, y_0^+ = 11.17$; (*b*) $T^+ = 100, t_f^+ = 10, y_0^+ = 6.52$.

streak-spacing comparisons inconclusive. It is, nevertheless, instructive to consider these comparisons in more detail.

In the DNS, the streak spacing was determined using a premultiplied spanwise energy spectrum $\Phi(\lambda_z) = (1/\lambda_z)E(\lambda_z)$, at a given distance from the wall, where E is the standard energy spectrum dependent on the spanwise wavelength λ_z. The value of λ_z at which Φ has a maximum is taken as the streak spacing. In the case without wall oscillation and in the vicinity of the wall, Φ has a maximum at about $\lambda_z^+ = 100$, which corresponds to the generally accepted average streak spacing. In the case of an oscillating wall, the phase-averaged spectrum was used, so that the streak spacing is time-dependent. The streak spacing obtained from the GOP approach is also time-dependent, since the optimal perturbation depends on t_f.

Two representative examples of pre-multiplied spectra obtained by DNS are given in figure 4. Figure 4(*a*) represents the most common case, when there is a maximum at a wavelength corresponding to the near-wall streak spacing. However, in a few cases, all for $T^+ = 100$ when the drag reduction is large, and during the part of the oscillation period when the near-wall streaks are barely detectable, the pre-multiplied spectrum is similar to figure 4(*b*). In these cases the near-wall streaks are so weak that the spectrum is dominated by the large-scale structures. Such cases will be omitted from the comparisons to follow. Their occurrence can be recognized by the gaps in the numerical data.

The spectra in the main flow direction have similar behaviour to that in the spanwise direction, but the situation when the maximum is at large values of λ_x is more common. This might correspond not only to the cases when the outer structure dominates, but also to the cases when the streak angle is small. For this reason, no data were discarded on the basis of the analysis of the longitudinal spectrum, even though some of the results can in fact be affected by outer structures.

Determining both characteristic spanwise and streamwise scales allows the streak-angle magnitude $|\theta| = \arctan \lambda_z/\lambda_x$ to be calculated, but not its sign. The sign has to be determined visually, and this is not always possible, as some of the visualizations do not show clear streaks. In the figures to follow the points for which the angle sign could be determined are shown with open symbols, while other points are shown with filled symbols. This is more important for the angle comparisons discussed in the

https://doi.org/10.1017/jfm.2013.165 Published online by Cambridge University Press

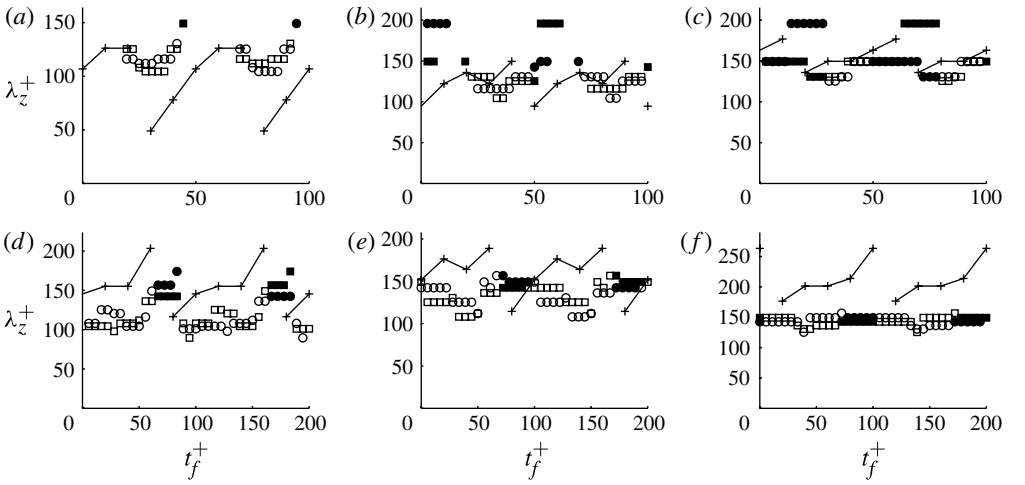


FIGURE 5. Streak spacing obtained from DNS (symbols) and $\boldsymbol{u}_{gop}$ (lines): (*a*) $T^+ = 100$, $y_0^+ \approx 7$; (*b*) $T^+ = 100$, $y_0^+ \approx 11$; (*c*) $T^+ = 100$, $y_0^+ \approx 16$; (*d*) $T^+ = 200$, $y_0^+ \approx 7$; (*e*) $T^+ = 200$, $y_0^+ \approx 11$; (*f*) $T^+ = 200$, $y_0^+ \approx 16$. Solid symbols are for cases when streak angle cannot be determined from the DNS, open symbols are for cases when the angle can be determined. Squares show the streak spacing extracted from the DNS phase-averaged premultiplied spectrum. Circles are the same as the squares but shifted by half a period.

next section. Here, it is sufficient to know that open symbols are for cases with clear streaks, while filled symbols are for cases when the streaks are not very apparent.

Due to the left–right symmetry of the wall motion, the streak spacing should be a periodic function of time, with the period equal to one half of the wall-oscillation period. However, since the maximum in the DNS spectra is often indistinct, the numerical data do not have this property, and the difference between the streak spacing obtained at values of time separated by half an oscillation period may indicate the magnitude of the numerical error. For this reason we plot each data point twice, the second time with a half-period shift. The GOP results satisfy the symmetry property exactly.

Figure 5 shows comparisons of streak spacing for $T^+ = 100$, that is in the regime with largest drag reduction, when streaks are difficult to detect, and for $T^+ = 200$. Note that the spectrum features noticeable fluctuations. Removing these fluctuations would require phase-averaging over many more periods than was possible. This led to streak spacing often having the same value for several consecutive instants. This is a purely numerical artefact. Several observations can be made. First, the discrepancy between the streak spacing of $\boldsymbol{u}_{gop}$ and the DNS results is, in some instances, as large as 50 %, which is the same order of magnitude as the variation of the streak spacing with time and distance from the wall. Given the approximate nature of the filtering effect, such a discrepancy is not unexpected. Comparing the characteristic peak width in the λ_z direction for oscillating and non-oscillating cases in figure 3, one can see that the degree of uncertainty (the ratio of the passband width to the passband midpoint) is similar for both. This uncertainty, combined with only a small variation in the numerically computed streak spacing, does not allow conclusions to be drawn. This is different from the situation in Chernyshenko & Baig (2005), where the discrepancy was mostly within 30 %, while the variation of streak spacing over all cases considered

https://doi.org/10.1017/jfm.2013.165 Published online by Cambridge University Press

was more than 1000 %. Certain trends are shared by the GOP and the numerical results. As the distance from the wall increases, the streak spacing increases. The streak spacing experiences a jump in GOP results within that part of the period when streaks are more difficult to identify in the DNS results. These observations neither contradict nor strongly support the theoretical approach: the basis for comparisons is simply too narrow, and the existence of two peaks of the amplification factor further complicates the considerations. Fortunately, the comparisons for the streak angle are more informative.

4.5. *Streak angles*

Calculations of the streak angle were performed for several distances from the wall and for several values of the oscillation phase. For each case, the energy spectrum in the main flow direction, premultiplied with $1/\lambda_x$, and the premultiplied energy spectrum in the spanwise direction (as in figure 4) were calculated. Then, the maxima of each were found, thus giving the longitudinal λ_x and spanwise λ_z wavelengths. The values obtained were treated as reliable only in cases where a maximum in the pre-multiplied spectrum was present for both $\lambda_z^+ < 300$ and $\lambda_x^+ < 600$. This eliminates a contamination by the footprints of the large-scale structures when the streaks are not energetic enough.

In all cases where both the values λ_x^+ and λ_z^+ were judged reliable, the streaks could be easily recognized in related visualizations. For these points, the absolute value of the angle could be obtained as $|\theta| = \arctan \lambda_z/\lambda_x$ directly from the positions (λ_x, λ_z) of the maxima, and its sign was determined from the flow visualization. All cases in which streaks are indistinct or are absent from visualizations correspond to the cases when at least one of the premultiplied spectrum plots has no clear local maximum. Only cases with $\lambda_z^+ > 300$ were completely ignored. When $\lambda_x^+ > 600$, the streaks are usually difficult to observe. It is then also difficult to visually identify the sign of the angle. However, the absolute value of the angle can still be extracted from the spectrum. Such points are included in the comparisons twice, with plus and minus sign, and are shown with filled symbols. The $\boldsymbol{u}_{gop}$ angles are much easier to extract, as the structures are infinitely long in one direction and well defined if the convergence of the optimization algorithm is good enough. However, they become less reliable when their absolute value is small, because the streamwise wavelength of $\boldsymbol{u}_{gop}$ might become comparable to, or even longer than, the numerical domain. Due to the left–right symmetry of the mean flow, the absolute value of the angle is a periodic function of time with the period equal to one half of that of the wall oscillations. The DNS results deviate from this because the phase-averaging could be done only over a finite time interval. Hence, similarly to the streak-spacing plot, each DNS point is plotted twice with a half-period and a sign shift. The discrepancy between the points gives an estimate of the magnitude of the averaging error.

Angle comparisons were done for a large number of cases (different oscillation periods and distances from the wall). Some of the results are shown in figure 6. Because streaks are less discernible in the case $T^+ = 100$, there are fewer computational points for this case than for $T^+ = 200$. Note the discontinuity of the predicted angle as a function of the phase t_f^+. The jump occurs when one local maximum of $A_0(t_i, \lambda_z, t_f)$ becomes higher than the other, so that the global maximum switches (compare figure 3*b,c* with figure 6*c*). It is also worth noting that between the jumps the angle variation remains limited. This feature will be discussed in more detail in § 5. Overall, the comparisons of the angle are favourable.

https://doi.org/10.1017/jfm.2013.165 Published online by Cambridge University Press

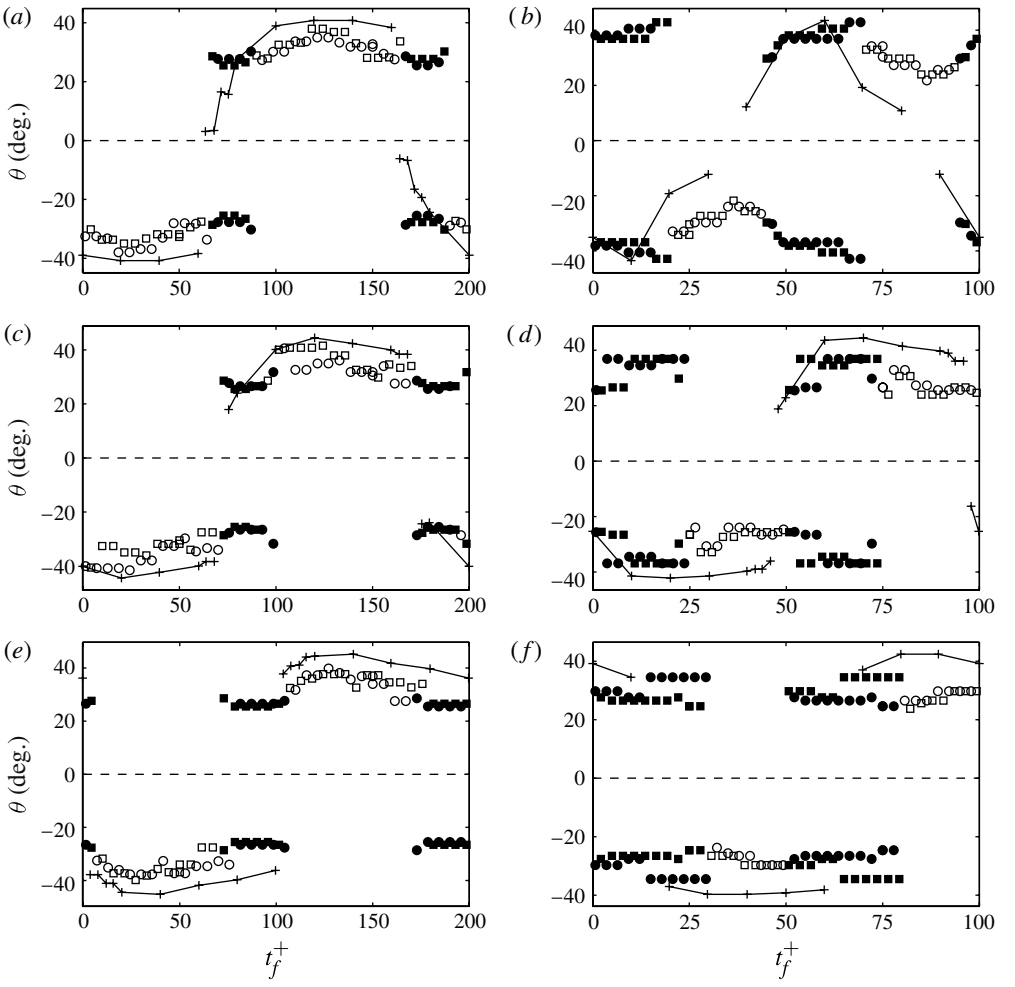


FIGURE 6. Streak angle θ as a function of the oscillation phase: DNS (symbols) at $Re_\tau = 500$, GOP (lines) at $Re_\tau = 180$. Squares show the angle extracted from the DNS phase-averaged premultiplied spectrum. Circles are the same as the squares but shifted by half a period and with the opposite sign. The symbols are filled when the sign of the angle could not be determined from the visualizations. (*a*) $T^+ = 200$, $y_0^+ = 7.5$, $y_{DNS}^+ = 6.5$; (*b*) $T^+ = 100$, $y_0^+ = 7.5$, $y_{DNS}^+ = 6.5$; (*c*) $T^+ = 200$, $y_0^+ = 11.2$, $y_{DNS}^+ = 11.2$; (*d*) $T^+ = 100$, $y_0^+ = 11.2$, $y_{DNS}^+ = 11.2$; (*e*) $T^+ = 200$, $y_0^+ = 17$, $y_{DNS}^+ = 16$; (*f*) $T^+ = 100$, $y_0^+ = 17$, $y_{DNS}^+ = 16$.

4.6. *Conditional-average comparison*

The filtering idea suggests that, in general, the output of an optimal perturbation can, while the input cannot, be expected to be similar to the structures observed in the real flow. For example, if the optimal perturbation were obtained by maximizing a measure of longitudinal vorticity instead of velocity, as was suggested in Chernyshenko & Baig (2005), then comparing vortices of such an optimal perturbation with vortices in the turbulent flow would be justified, but not comparing streaks. For the particular form of the optimal perturbation considered here, streaks can be compared while vortices

https://doi.org/10.1017/jfm.2013.165 Published online by Cambridge University Press

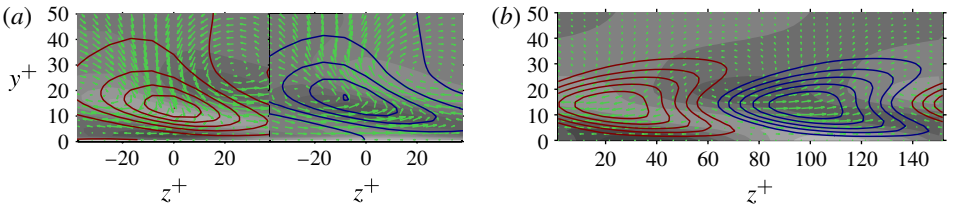


FIGURE 7. (Colour online) Comparison of (*a*) DNS conditional average based on sampling at $y^+ = 13$ and (*b*) $\boldsymbol{u}_{gop}$ at $y_0^+ = 11$ (see (2.4)), both for $T^+ = 200$ at phase $t_f^+ = 0$. Contour lines are streamwise velocity isolines, arrows represent the cross-flow velocity, and the background grey shades represent the streamwise vorticity. For comparison, the flow fields were normalized so that the maximum streamwise velocity is equal to 1 in each case.

cannot. This is valid as far as the instantaneous characteristics of the turbulent flow are concerned.

In contrast to instantaneous fields, there is a possibility that not only the outputs, but also the inputs of the optimal perturbation can be similar to the structure of a conditional average, provided that the conditional sampling of the turbulent flow is triggered by the same quantity that is maximized when the optimal perturbation is calculated, and that certain assumptions about the right-hand side $\boldsymbol{F}$ of (2.1) are valid. To illustrate this idea, consider the following simple model.

Let $\hat{\boldsymbol{u}} = \boldsymbol{L}\hat{\boldsymbol{f}}$, where $\hat{\boldsymbol{u}} = (\hat{u}_1, \hat{u}_2)$ and $\hat{\boldsymbol{f}} = (\hat{f}_1, \hat{f}_2)$ are two-dimensional vectors and $\boldsymbol{L} = \{L_{ij}\}$ is a 2×2 matrix, so that $\hat{u}_i = L_{ij}\hat{f}_j$. Let the optimal perturbation be defined as such $\hat{\boldsymbol{f}}$ of a unit length that $\hat{u}_1$ is maximized. Then, $\hat{\boldsymbol{f}}_{opt} = (L_{11}, L_{12})/\sqrt{L_{11}^2 + L_{12}^2}$. Now, let $\hat{\boldsymbol{f}}$ be a random vector represented by a statistical ensemble of its realizations. Let us assume that the probability density function of $\hat{\boldsymbol{f}}$ is constant inside the circle $|\hat{\boldsymbol{f}}| = f_{max}$ and is zero outside. This means that all directions of $\hat{\boldsymbol{f}}$ are equally probable, while the magnitude of $\hat{\boldsymbol{f}}$ is bounded by f_{max}. Accordingly, in all realizations, $\hat{u}_1 < \hat{u}_{1,max} = \sqrt{L_{11}^2 + L_{12}^2} f_{max}$. Next, let this statistical ensemble be conditionally averaged on $\hat{u}_1 > (1 - \epsilon)\hat{u}_{1,max}$, where $\epsilon \ll 1$. This means that all the realizations for which $\hat{u}_1 < (1 - \epsilon)\hat{u}_{1,max}$ are discarded, and the remaining realizations are averaged to give the conditionally-averaged $\hat{\boldsymbol{f}}$. Since the condition can be satisfied only for those $\hat{\boldsymbol{f}}$ that are almost parallel to $\hat{\boldsymbol{f}}_{opt}$, the conditionally-averaged $\hat{\boldsymbol{f}}$ will also be almost parallel to $\hat{\boldsymbol{f}}_{opt}$. That is, the conditional average and the optimal perturbation, multiplied by a suitable constant, almost coincide.

This model shows that if a randomly forced linear operator is considered, the optimal perturbation can be similar to the conditionally-averaged picture. In a real turbulent flow, however, the nonlinear terms represented by $\boldsymbol{F}$ in (2.1) have a much more complex behaviour. Generalizing the simple model described here to turbulent flow would be too difficult, and no attempt to do so is made here. The above argument gives motivation for a comparison of $\boldsymbol{u}_{gop}$ with a conditional average of the turbulent flow field, in order to see if this idea deserves further development.

Conditional averaging was triggered by extrema of the longitudinal velocity. The sampling threshold was high enough for the conditionally-averaged structures to be meaningful, and low enough to allow for large samples and good convergence (more details can be found in Touber & Leschziner 2012). Figure 7 shows a comparison representative of the part of the period when streaks are more pronounced (open

https://doi.org/10.1017/jfm.2013.165 Published online by Cambridge University Press

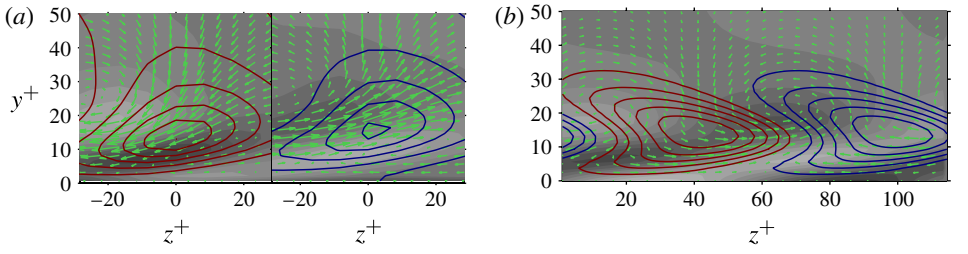


FIGURE 8. (Colour online) As figure 7 but at phase $t_f^+ = 80$.

symbols in figure 6*c*). For $y^+ < 20$, there is a good qualitative agreement between the shape of the streaky structures and the cross-flow velocity field and vorticity. For $y^+ > 20$, the figures differ significantly. This could be the result of a partial visualization of the outer-layer structures, due to the correlation between the streaks and these structures in the DNS, which is not accounted for in the GOP analysis.

For phases close to values at which the angle jump occurs, the agreement is poor (see figure 8). This is expected and has a similar origin to that of the angle discontinuity. Close to the angle-jump position, there are two possible dominant structures, corresponding to the two peaks in figure 3(*b,c*). Both structures should be present in DNS results, whereas only the most energetic one will be obtained with the GOP approach. As a result, the conditional-average picture will be a combination of the two dominant structures, but the GOP will contain only one of them.

5. The mechanism of the generalized optimal perturbation for the flow past an oscillating wall

So far, attention has focused on the properties of $\boldsymbol{u}_{gop}$ at $t = t_f$, which, being the filter output, can be meaningfully compared with the real flow. The behaviour of $\boldsymbol{u}_{gop}$ at $t < t_f$ is also of interest since its analysis helps to understand the filtering properties of the linearized Navier–Stokes operator. This is the subject of the present section.

An optimal perturbation is a three-dimensional time-dependent solenoidal vector field satisfying the linearized Navier–Stokes equations. It is natural to describe this field as a fluid flow. However, to avoid any misunderstanding, we reiterate (see § 2.1) that this velocity field should not be considered as a model of a turbulent flow or an approximation to it, even though certain features (only those corresponding to the output maximized by the GOP) can be expected to be similar. The flows considered in this section are only tools used to understand, via its GOP solutions, the properties of the linearized Navier–Stokes operator for the case of a flow past a spanwise-oscillating wall.

5.1. *Universal optimal solution*

The filtering properties of the linearized Navier–Stokes operator determining $\boldsymbol{u}_{gop}$ depend on the distance between the wall and the observation plane y_0^+, and on the observation phase t_f^+ where and when the energy amplification coefficient is maximized. Here, we will set the distance from the wall and will first study the dependence of $\boldsymbol{u}_{gop}$ on t_f^+, before analysing the temporal evolution of $\boldsymbol{u}_{gop}$ to understand the formation mechanisms.

https://doi.org/10.1017/jfm.2013.165 Published online by Cambridge University Press

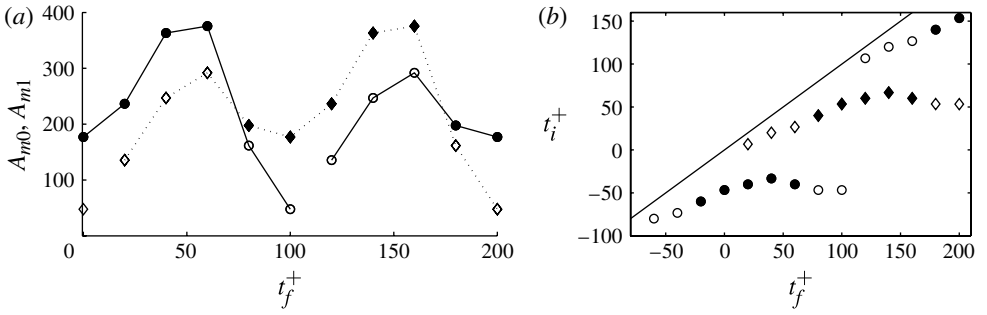


FIGURE 9. (*a*) Temporal evolution of the local peaks of $A_0(t_f, t_i, \lambda_z)$ (see figure 3) as a function of the observation phase t_f^+; $Re_\tau = 180$, $T^+ = 200$, and $y_0^+ = 11.25$. The global optimum $A_{m0}(t_f^+) = \max_{t_i,\lambda_z} A_0(t_f, t_i, \lambda_z)$ is shown with filled symbols, and the secondary maximum, denoted A_{m1}, is shown with open symbols. Points corresponding to the same local peak (peaks grouped by similar values of the initial time t_i) are connected with lines. (*b*) Dependence of the initial time on the finite time for the local peaks.

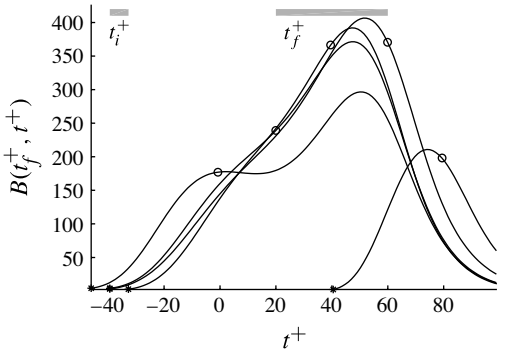


FIGURE 10. Temporal evolution of $B(t_f, t) = \|\boldsymbol{u}'(t)\|_f^2 / \|\boldsymbol{u}'(t_i)\|_i^2$ for five values of t_f^+ regularly spaced over half a period. The points $(t_f, B(t_f, t_f)) = (t_f, A(t_f))$ are marked with $\circ$ and the points $(t_i, B(t_f, t_i))$ are marked with $*$. The grey bars show the variation of t_i^+ and t_f^+ for $\boldsymbol{u}_{gop}$ close to the universal optimal. $Re_\tau = 180$, $T^+ = 200$, and $y_0^+ = 11.25$.

Figure 9 shows the dependence of selected filter properties on the phase. It illustrates the characteristics of the perturbations corresponding to the two local maxima of the energy-amplification-coefficient map (see again figure 3*b–d*, the global maximum corresponding to $\boldsymbol{u}_{gop}$). One can clearly see how the global maximum switches between the two local maxima. The curves corresponding to the different local maxima are similar, and indeed differ only by a phase shift equal to half a period. This suggests that the curves represent the same object, appearing repeatedly with a mirror (left/right) symmetry and with a half-period shift. This is natural since the base flow itself has such symmetry.

Figure 9(*b*) shows that, when the local peak is also a global maximum (filled symbols), the corresponding t_i remains relatively constant. This suggests that the filter properties are similar for a range of t_f^+. Figure 10 shows, for several values of t_f^+, the energy amplification factor $B(t_f, t) = \|\boldsymbol{u}'(t)\|_f^2 / \|\boldsymbol{u}'(t_i)\|_i^2$ as a function of time, each curve starting at its initial time t_i^+, evolving to the time t_f^+ for which this perturbation

https://doi.org/10.1017/jfm.2013.165 Published online by Cambridge University Press

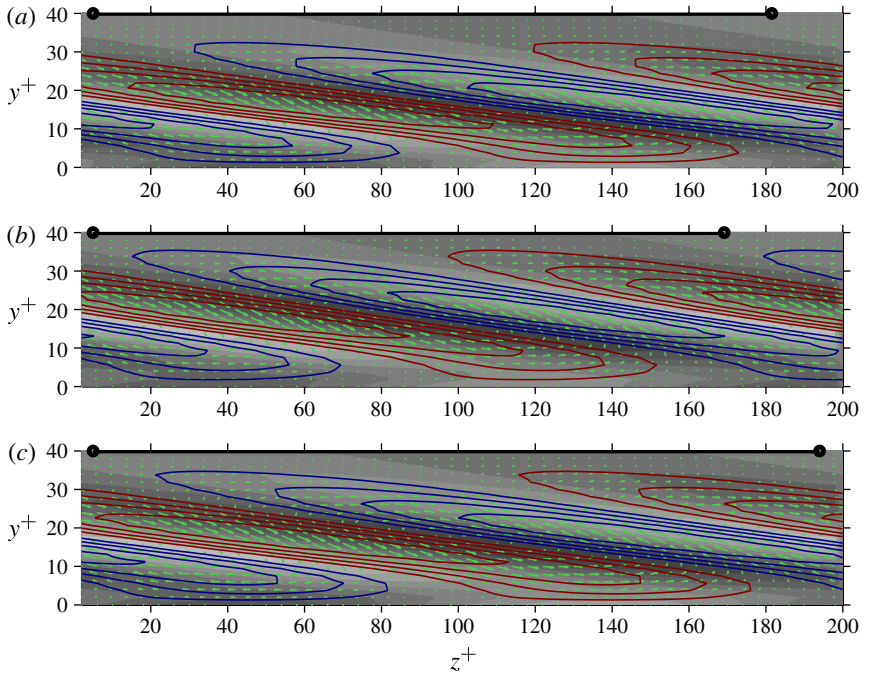


FIGURE 11. (Colour online) Initial conditions of three optimal $\boldsymbol{u}_{gop}$ close to the 'universal optimal' (compare with figure 10): (*a*) $t_f^+ = 20$, $t_i^+ = -39.4$, $\lambda_z^+ = 177$; (*b*) $t_f^+ = 40$, $t_i^+ = -32.8$, $\lambda_z^+ = 164$; (*c*) $t_f^+ = 60$, $t_i^+ = -39.4$, $\lambda_z^+ = 189$. Contours are the isolines of the streamwise velocity, arrows are the cross-flow velocity, and the background grey shades represent the streamwise vorticity. Note that the spanwise wavelength, shown with a thick black line on top of each graph, is not exactly the same for these three cases.

is the optimal (so that $A(t_f) = B(t_f, t_f)$), and then continuing to higher t and eventually decaying. It turns out that certain perturbations originating in a relatively narrow area (the initial time t_i^+ corresponding to these perturbations varies by only $\Delta t_i^+ \approx T^+/20$) of the oscillation half-period experience a very fast growth. As a result, when an optimization of the energy amplification at different values of t_f^+ is done, the optimal initial time to introduce this perturbation happens to be somewhere within this interval, and the optimal perturbation itself (and this includes its angle) remains approximately the same. This is further illustrated in figure 11, showing the initial conditions for three optimal solutions with different t_f^+. This explains the limited variation of the streak angle between the jumps.

Hence, the overall picture can now be described in a simple way. Apart from a limited transition interval between the jumps, $\boldsymbol{u}_{gop}$ remains roughly the same for all t_f^+. It evolves by the same mechanism and can be represented by one universal optimal perturbation. The universal optimal perturbation dominates half of the oscillation period and then gives way to another universal optimal perturbation, shifted in phase by half a period and with the angle of the opposite sign.

5.2. *The main energy content of the universal generalized optimal perturbation*

The universal-optimal-perturbation structure is infinitely long in one direction, and this direction does not vary in time. If this pattern is studied in a frame of reference

https://doi.org/10.1017/jfm.2013.165 Published online by Cambridge University Press

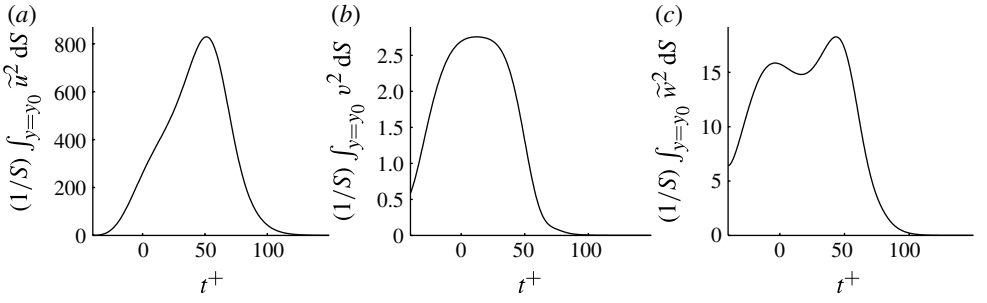


FIGURE 12. Time evolution of (*a*) $\widetilde{u}^2$, (*b*) v^2 and (*c*) $\widetilde{w}^2$, averaged over the plane $y = y_0$ for one optimal perturbation. The norm of the initial condition $\|\boldsymbol{u}'\|_i = 1$. $T^+ = 200$, $Re_\tau = 180$, $y_0^+ = 11.25$ and $t_f^+ = 60$.

where $\widetilde{x}$ is aligned with the streak direction, $\widetilde{z}$ is orthogonal to it and parallel to the wall, with the wall-normal direction y being the third coordinate, the linearized Navier–Stokes equations become simpler. In this new frame of reference all variables are independent of $\widetilde{x}$, and therefore their derivatives with respect to $\widetilde{x}$ vanish. The momentum equations then take the form:

$$\frac{\partial \widetilde{u}}{\partial t} + \widetilde{W}\frac{\partial \widetilde{u}}{\partial \widetilde{z}} + v\frac{\partial \widetilde{U}}{\partial y} = \frac{1}{Re}\Delta\widetilde{u}, \tag{5.1a}$$

$$\frac{\partial v}{\partial t} + \widetilde{W}\frac{\partial v}{\partial \widetilde{z}} = -\frac{\partial \widetilde{p}}{\partial y} + \frac{1}{Re}\Delta v, \tag{5.1b}$$

$$\frac{\partial \widetilde{w}}{\partial t} + \widetilde{W}\frac{\partial \widetilde{w}}{\partial \widetilde{z}} + v\frac{\partial \widetilde{W}}{\partial y} = -\frac{\partial \widetilde{p}}{\partial \widetilde{z}} + \frac{1}{Re}\Delta\widetilde{w}, \tag{5.1c}$$

where $\widetilde{u}$ and $\widetilde{w}$ are the components of the perturbation velocity in the new frame of reference, and both mean velocities $(\widetilde{U}, \widetilde{W})$ are now time-dependent, representing a combination of the turbulent mean profile and the Stokes layer. The continuity equation has the form $\partial v/\partial y + \partial \widetilde{w}/\partial \widetilde{z} = 0$. Note that (5.1*b*,*c*) representing the cross-flow evolution are independent of (5.1*a*).

The universal optimal perturbation will be exemplified here by $\boldsymbol{u}_{gop}$ for $t_f^+ = 60$, $y_0^+ = 11.25$, and for the wall-oscillation period $T^+ = 200$. Figure 12 shows the time evolution of the contribution of each velocity component to the energy of this perturbation. The surface energy norm of the $\widetilde{x}$-component is greater than the surface energy norm of the x-component (compare with figure 10), and much greater than the magnitude of the other two components, that is the wall-normal and cross-flow components. Hence, including or omitting other velocity components in the final norm is relatively unimportant. For example, if the final norm was defined as $u^2 + v^2 + w^2$ instead of just u^2 as it is the case in (2.4), $\boldsymbol{u}_{gop}$ would be almost the same, but with the energy curve similar to figure 12(*a*) instead of figure 10.

The dominance of $\widetilde{u}$ also suggests that (5.1*a*) should be analysed first to understand the mechanism of energy amplification. Multiplying (5.1*a*) by $\widetilde{u}$ and integrating over the flow domain gives the energy equation in the form :

$$\frac{\mathrm{d}}{\mathrm{d}t}\int_V \frac{\widetilde{u}^2}{2}\,\mathrm{d}V + \int_V \widetilde{u}\,v(\partial\widetilde{U}/\partial y)\,\mathrm{d}V = -(1/Re)\int_V (\nabla\widetilde{u})^2\,\mathrm{d}V. \tag{5.2}$$

https://doi.org/10.1017/jfm.2013.165 Published online by Cambridge University Press

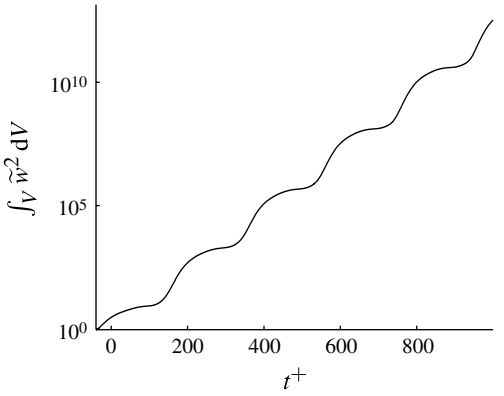


FIGURE 13. Floquet instability with $\widetilde{W}\partial/\partial z$ removed from (5.1).

The only term contributing to a potential increase in energy stems from $v\partial\widetilde{U}/\partial y$ in (5.1*a*). This term describes the well-known lift-up effect, which amounts to advection of the mean velocity by the wall-normal component of the velocity perturbation. In the case of an oblique pattern above an oscillating wall, the shear is time-dependent, and one can expect that the growth will be favoured during that part of the oscillation period when $\partial\widetilde{U}/\partial y$ is large. Another difference from the non-oscillating case is the presence of the similar term, $v\partial\widetilde{W}/\partial y$, in (5.1*c*). Because of this term there can also be a transient growth of the cross-flow velocity components, and this is indeed observed in figure 12(*b,c*).

5.3. *Effects of cross-flow advection of the perturbation and of energy transfer from mean spanwise flow to the perturbation*

In order to estimate the relative importance of various physical effects, calculations were performed with some of the terms removed from the governing equations. First, we removed the terms involving $\widetilde{W}\partial[\ldots]/\partial\widetilde{z}$ in (5.1). These describe the effects of cross-flow advection of the perturbation. It turned out that the linearized operator becomes unstable without these terms, and the solution diverges along a Floquet orbit, see figure 13. This shows that these terms have a crucial stabilizing effect, and that analysing the Navier–Stokes equations by removing some of its terms is not always straightforward.

Removing $v\partial\widetilde{W}/\partial y$ from (5.1*c*) reduces substantially (from 800 to 30) the growth of $\widetilde{u}$, see figure 14. This term is responsible for energy transfer from the mean flow to the cross-flow component of the perturbation. Without it, the cross-flow volume-averaged energy decays monotonically with time. As has been shown in § 5.2, the cross-flow contributes to the final norm only indirectly, via the lift-up mechanism. This indirect effect is more properly measured by the volume-averaged energy of the cross-flow than by its plane average, and for this reason the figure shows the plane average for $\widetilde{u}^2$, but volume averages for v^2 and $\widetilde{w}^2$. The system is now very similar to the non-oscillating case, and the scenario for the transient energy growth is well understood. Note again that, at the start, more than 95 % of the flow energy is concentrated in the cross-flow components (since the same initial condition is considered). With time, the cross-flow energy decreases monotonically due to the action of viscosity. At the same time, the wall-normal component triggers the transient growth of the streamwise

https://doi.org/10.1017/jfm.2013.165 Published online by Cambridge University Press

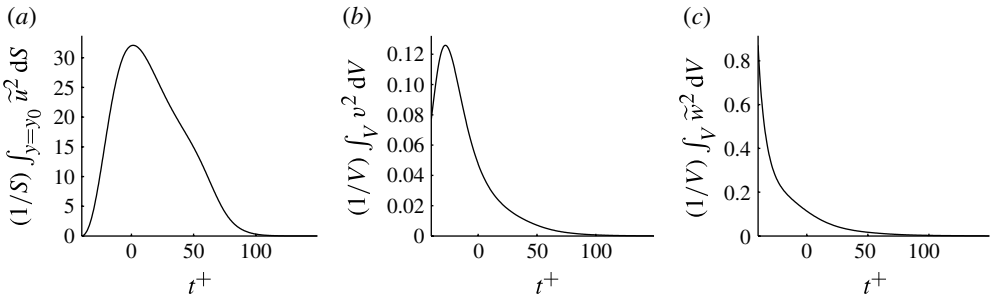


FIGURE 14. Effect of removing $v\partial\widetilde{W}/\partial y$ from (5.1*c*): (*a*) plane average of $\widetilde{u}^2$; (*b*) volume average of v^2; (*c*) volume average of $\widetilde{w}^2$.

component via the term $v\partial\widetilde{U}/\partial y$, and this process stops once the velocity v becomes too small. Notably, the growth is much smaller than in the case of the full equation, which suggests that the transient growth of the cross-flow is important.

5.4. *The cross-flow transient growth is caused by the Orr mechanism*

The temporal evolution of the volume average of v^2 and $\widetilde{w}^2$ for the universal optimal perturbation (no terms removed) is shown in figure 15(*a,b*). In the frame of reference aligned with the streaks, the equations for v and $\widetilde{w}$ are independent of the equation for $\widetilde{u}$, so that the flow is essentially two-dimensional. This suggests that the transient growth might be caused by the well-known Orr mechanism (Farrell & Ioannou 1993*a*). This is further supported by the observation that, at the start, the volume average of the wall-normal-velocity squared is small compared to the volume average of $\widetilde{w}^2$. Figure 16 leaves little doubt: one can clearly see that at the start of the motion the vorticity is organized in sheets inclined against the mean shear (figure 16*a*). The shear then rotates the lines of the constant phase of the vorticity and, as the distance between the vorticity sheets increases, they induce larger velocity, which is the Orr mechanism. Further rotation decreases the vorticity sheet separation, and the velocity induced by the vorticity distribution decreases again. Viscous diffusion, the vicinity of the wall, and the time-dependence and non-uniformity of shear all contribute, making the picture more complicated, but the main features of the Orr mechanism are clearly there.

Overall, one may conclude that the transient growth of the universal $\boldsymbol{u}_{gop}$ is a combination of the transient growth due to the Orr mechanism in the plane perpendicular to the streaks and the mechanism of lift-up of the longitudinal mean velocity by this transient cross-flow. An excellent description of such a combination of mechanisms was given by Farrell & Ioannou (1993*a*), who considered a uniform time-independent shear, which allowed them to obtain analytical solutions. In that case the optimal perturbation was aligned with shear and had a pure lift-up mechanism. In order to reveal the interplay between the Orr and lift-up mechanisms, Farrell & Ioannou fixed the inclination angle, thus considering a sub-optimal perturbation. In the case considered in the present work the direction of shear varies with time, so that the optimal perturbation is necessarily oblique and the interplay is always present. Another difference is that we studied generalized optimal perturbations.

https://doi.org/10.1017/jfm.2013.165 Published online by Cambridge University Press

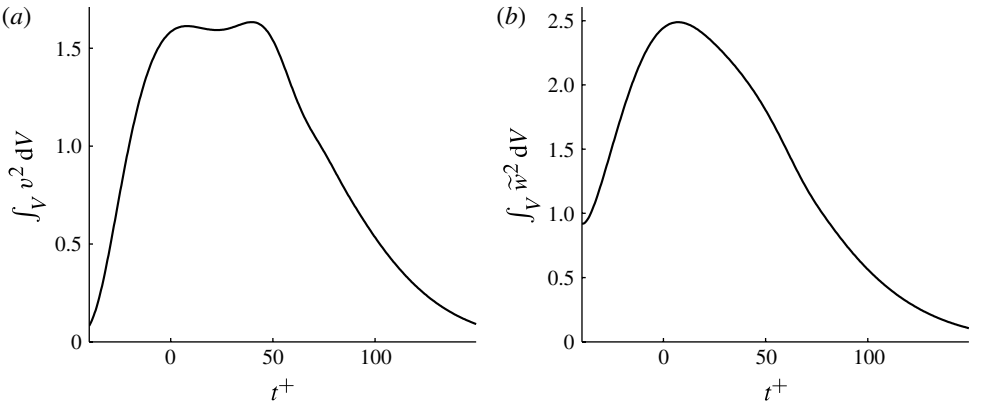


FIGURE 15. Volume average of the cross-flow velocity components v^2 and $\widetilde{w}^2$, in a frame of reference linked to the streaks for the universal $\boldsymbol{u}_{gop}$.

6. Conclusions

The study has shown that salient structural features of the response of the turbulent near-wall layer to transverse oscillatory wall motion can be elucidated by way of a linear analysis of the Navier–Stokes equations. In particular, the analytical framework of the generalized optimal perturbation (GOP) approach applied in this work has yielded statements on the response of the streak properties and energy norms to the actuation, and comparisons with DNS data give credibility to the fundamental correctness of the analysis. Specific findings arising from the study are given in the following list.

(*a*) The GOP approach applied without using any data about the turbulent flow past a spanwise-oscillating wall was demonstrated to give results in reasonable agreement with DNS.

(*b*) For the flow past a spanwise-oscillating wall, the generalized optimal perturbation ($\boldsymbol{u}_{gop}$) was found to be an infinitely long structure having a certain angle to the mean flow direction. The angle varies slowly with phase for half a period, and at a certain instant in the oscillation period changes discontinuously, changing its sign and magnitude.

(*c*) For almost any phase within the oscillation period, $\boldsymbol{u}_{gop}$ was shown to be close to a certain universal generalized optimal perturbation. This explains the limited variation of the streak angle between the jumps observed in DNS.

(*d*) The sudden jump of the streak angle is linked to the symmetry of the mean flow over half a period, as well as to the presence of the universal optimal perturbation. A universal optimal perturbation dominates the flow during a half-period, imposing a relatively constant angle. Because of the mean flow symmetries an identical universal optimal, but with the angle of opposite sign, dominates the flow during the following half-period. The jump occurs when the energy of one universal optimal becomes bigger than the energy of the previous one.

(*e*) During those parts of the oscillation period when the angle can be reliably extracted from DNS it matches approximately the angles predicted by the GOP theory. Near the jump position, the two dominant structures are superimposed with similar amplitude, which explains why it is difficult to observe streaks in the velocity fields obtained from DNS for this part of the period.

https://doi.org/10.1017/jfm.2013.165 Published online by Cambridge University Press

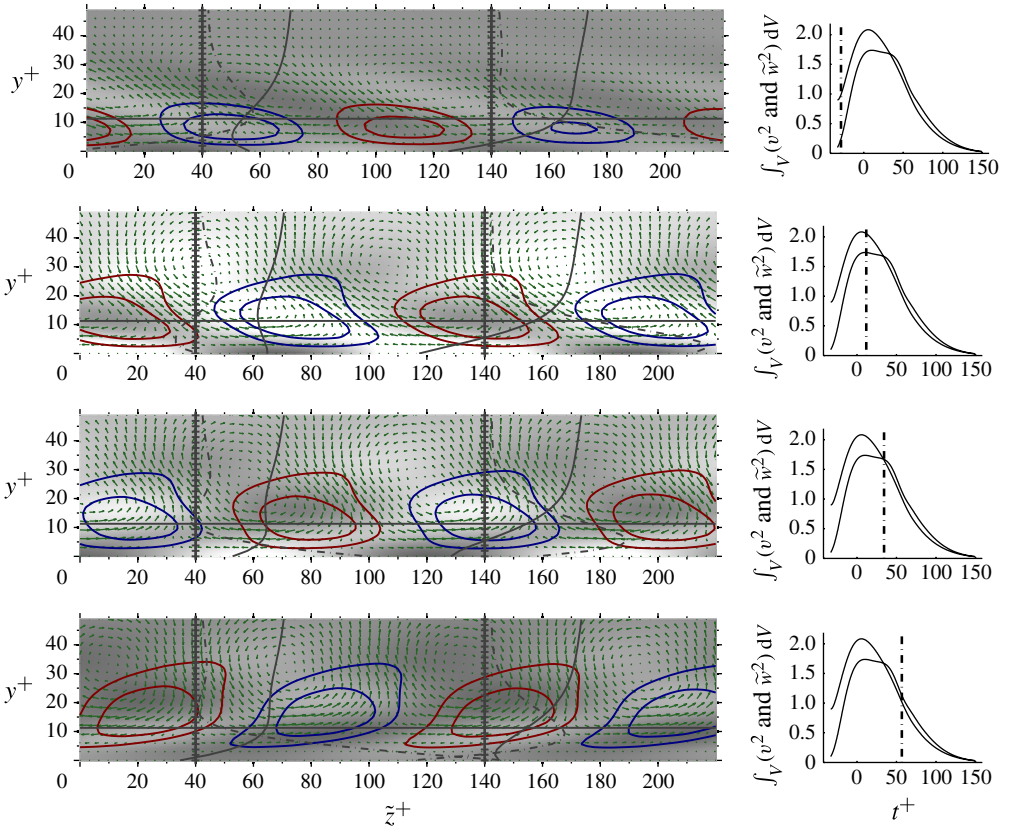


FIGURE 16. (Colour online) Evolution of the universal $\boldsymbol{u}_{gop}$ in the frame of reference linked to the streak. The horizontal straight line marks the layer $y = y_0$. Vectors show the cross-flow velocity. Grey shades show $\widetilde{x}$-component of vorticity. Closed solid contours are the contours of constant $\widetilde{u}$. The base flow components $\widetilde{U}$ and $\widetilde{W}$ are shown with solid curves, and their derivatives by the dashed curves. In the plots on the right the phase is marked with a vertical dot-dashed line, and the curves are the cross-flow energy components.

(*f*) The spanwise spacing between streaks was compared for all the flow cases available in DNS and GOP results, and this was shown to be of the same order of magnitude. The range of variation of streak spacing in DNS results is, however, of the same order as the error that can be reasonably expected from the GOP approach.

(*g*) The amplification factor of $\boldsymbol{u}_{gop}$ for oscillating wall cases was found to be significantly greater than its value for the non-oscillating wall. Hence, there is no direct link between this factor and the magnitude of the drag reduction. Some other measures of streak magnitude obtainable within the GOP paradigm were found to work better; however, drag reduction magnitude analysis is outside the scope of the present paper, and the present results in this respect are superseded by the findings of Duque-Daza *et al.* (2012) and Moarref & Jovanović (2012).

(*h*) The transient growth mechanism of the $\boldsymbol{u}_{gop}$ is found to be a combination of the Orr mechanism due to the cross-flow shear, acting at the initial stage, and the mechanism of the lift-up of the longitudinal velocity by longitudinal vortices,

https://doi.org/10.1017/jfm.2013.165 Published online by Cambridge University Press

acting at the later stage. The conditions for the Orr mechanism appear to exist only for a relatively short interval within the period, thus explaining why all optimal perturbations originate at approximately the same instant in the half-period, leading to the existence of the universal optimal perturbation.

Overall, the results obtained provide an insight into the pattern formation in turbulent flows near a spanwise-oscillating wall. Hopefully, this insight will be useful in improving the methods of turbulent skin friction reduction.

Acknowledgements

The authors are thankful to Dr S. Lardeau for providing the Navier–Stokes solver that formed the basis for developing the code using in the present work. The authors would like to acknowledge the financial support from EPSRC through grant EP/G060215/1, together with Airbus Operations Ltd and EADS UK Ltd.

Appendix. Numerical method

A.1. *Linear Navier–Stokes solver*

The linearized Navier–Stokes solver used in the present study was developed on the basis of an incompressible Navier–Stokes solver (Laizet & Lamballais 2009), which uses a finite difference approximation on a Cartesian grid. The spatial derivatives are based on a sixth-order compact scheme inside the domain (second-order at the boundary), the marching in time is done via a third-order low-storage Runge–Kutta scheme, and the Poisson solver is working in Fourier space, using fast Fourier transform for transformations between the physical space and the Fourier space. This solver can be used for various configurations for two-dimensional or three-dimensional flows. The linearized solver developed in the present study was based on the two-dimensional channel-flow version of the solver.

The linearized Navier–Stokes solver allows calculation of a channel flow with a travelling-wave oscillating wall, with the wall velocity of the form $w_{wall} = W_0 \cos(\omega t + kx)$, where x is the coordinate in the main flow direction. In this case the phase-averaged velocity does not depend on the spanwise coordinate z. For this reason the solution of the linearized Navier–Stokes equation can be decomposed into Fourier modes in the spanwise direction, each mode evolving in time independently. Since the spanwise Fourier modes are orthogonal to each other in all the norms used to define generalized optimal perturbations, the generalized optimal perturbation will have a single spanwise wavenumber. In the present paper only wall velocity of the form $w_{wall} = W_0 \cos(\omega t)$ is considered. With this simpler condition, the perturbation velocity can also be decomposed into Fourier modes in x, although this was not used in the present study. The more generic solver was developed with the view to further research.

In the linearized Navier–Stokes solver the perturbation velocities and pressure were represented as the sum of trigonometric functions in the spanwise direction for any spanwise wavelength λ_z:

$$\boldsymbol{u}' = \boldsymbol{u}'_c \cos\left(\frac{2\pi}{\lambda_z} z\right) + \boldsymbol{u}'_s \sin\left(\frac{2\pi}{\lambda_z} z\right), \tag{A 1}$$

with $\boldsymbol{u}'_c$ and $\boldsymbol{u}'_s$ given on a two-dimensional Cartesian grid in the streamwise and wall-normal directions. This leads to six momentum equations for $\boldsymbol{u}'_c$ and $\boldsymbol{u}'_s$ and two Poisson equations for pressure. For simplicity of notation $\boldsymbol{u}'$ will now be referred

https://doi.org/10.1017/jfm.2013.165 Published online by Cambridge University Press

to as the solution for a given wavelength λ_z in the spanwise direction. Solving the optimization problem (2.6) can be done in two steps given by (4.1*a*)–(4.1*b*).

In the first step (4.1*a*) the initial time t_i, the observation phase t_f, and the spanwise wavelength λ_z are fixed, and for these parameters the most amplified initial solution $\boldsymbol{u}_i$ is found. In the second step (4.1*b*) optimization is performed over t_i and λ_z to find the generalized optimal perturbation for phase t_f. The second step is a simple optimization over the two parameters t_i and λ_z, and standard methods to perform such optimization are available. The remaining part of this appendix focuses on the first step of the optimization.

A.2. *Adjoint optimization for generalized optimal perturbations*

Various methods are available to calculate optimal solutions of the linearized Navier–Stokes equation with time-periodic base flow. One of the most appropriate methods is to use the Floquet theory (Schmid 2007). However, the adjoint optimization of the equation was preferred in this study because of the high numerical cost of using the Floquet theory for two-dimensional problems. Adjoint optimization is a well-known approach to solving optimization problems (Farrell & Moore 1991; Hill 1995; Luchini 2000; Schmid 2007; Biau & Bottaro 2009), but in the present case the use of different initial and final norms requires certain adjustment of the method. In the code the velocity components are approximated by elements of a finite-dimensional space (with elements of the space being the set of values on a Cartesian grid in the streamwise and wall-normal directions). The projection of $\boldsymbol{u}'(t_i)$ onto this finite-dimensional space will be denoted $\boldsymbol{u}_i$, and the projection of $\boldsymbol{u}'(t_f)$ will be denoted $\boldsymbol{u}_f$. We now consider the problem of finding $\boldsymbol{u}_i$ such that the ratio $\|\boldsymbol{u}_f\|_f / \|\boldsymbol{u}_i\|_i$ is maximized. As the problem is linear and in a finite-dimension space, the final velocity can be linked to the initial velocity by a linear operator, which we will denote $\boldsymbol{R}$:

$$\boldsymbol{u}_f = \boldsymbol{R}\boldsymbol{u}_i. \tag{A 2}$$

The initial norm is the usual energy norm, and it can be written using the scalar product as $\|\boldsymbol{u}_i\|_i^2 = \langle \boldsymbol{u}_i, \boldsymbol{u}_i \rangle$. If a linear operator $\boldsymbol{P}$ is defined as the projection operator onto the subspace of longitudinal velocity component in the layer $y = y_0$ then the final norm can be written as $\|\boldsymbol{u}_i\|_f^2 = \langle \boldsymbol{P}\boldsymbol{u}_i, \boldsymbol{P}\boldsymbol{u}_i \rangle$, with the scalar product taken in the subspace. Then the optimization problem can be formulated as

$$A_0 = \max_{\boldsymbol{u}_i} \frac{\langle \boldsymbol{P}\boldsymbol{u}_f, \boldsymbol{P}\boldsymbol{u}_f \rangle}{\langle \boldsymbol{u}_i, \boldsymbol{u}_i \rangle} = \max_{\boldsymbol{u}_i} \frac{\langle \boldsymbol{P}\boldsymbol{R}\boldsymbol{u}_i, \boldsymbol{P}\boldsymbol{R}\boldsymbol{u}_i \rangle}{\langle \boldsymbol{u}_i, \boldsymbol{u}_i \rangle} = \max_{\boldsymbol{u}_i} \frac{\langle \boldsymbol{u}_i, \boldsymbol{R}^*\boldsymbol{P}^*\boldsymbol{P}\boldsymbol{R}\boldsymbol{u}_i \rangle}{\langle \boldsymbol{u}_i, \boldsymbol{u}_i \rangle}, \tag{A 3}$$

where * denotes the adjoint operator. The optimization method is based on the observation that $\boldsymbol{R}^*\boldsymbol{P}^*\boldsymbol{P}\boldsymbol{R}$ is a symmetric matrix. Finding the most amplified initial solution $\boldsymbol{u}_i$ of the problem is equivalent to finding an eigenvector in the biggest eigenvalue subspace of $\boldsymbol{R}^*\boldsymbol{P}^*\boldsymbol{P}\boldsymbol{R}$. This suggests the following iterative method. A random initial guess $\boldsymbol{u}_0$ is chosen, so that it has a non-zero component in each eigenspace of the operator (including the one corresponding to the biggest eigenvalue). Then it can be shown that the sequence of the direction of $\boldsymbol{f}_n = (\boldsymbol{R}^*\boldsymbol{P}^*\boldsymbol{P}\boldsymbol{R})^n \boldsymbol{u}_0$ converges to a direction within the maximum eigenvalue subspace (the most amplified $\boldsymbol{u}_i'$ multiplied by some constant). Due to the properties of the sequence, it can be shown that the convergence is geometric. To find $\boldsymbol{f}_n$, and particularly its direction, the following algorithm was implemented.

Note that $\boldsymbol{R}$ corresponds to the linearized Navier–Stokes solver marching from t_i to t_f, $\boldsymbol{P}^* = \boldsymbol{P}$ is a simple projection, and $\boldsymbol{R}^*$ is the adjoint operator, an operator similar

https://doi.org/10.1017/jfm.2013.165 Published online by Cambridge University Press

to the linearized solver but which has to be solved backward in time from t_f to t_i. An iteration of the algorithm consists of four steps:

(*a*) $\boldsymbol{u}_i := \boldsymbol{u}_i / \|\boldsymbol{u}_i\|_i$ (renormalization at initial time t_i);

(*b*) $\boldsymbol{u}_f := \boldsymbol{R}\boldsymbol{u}_i$ (direct problem, solve the linearized equation to obtain the solution at final time);

(*c*) $\boldsymbol{u}_f := \boldsymbol{P}^*\boldsymbol{P}\boldsymbol{u}_f = \boldsymbol{P}^2\boldsymbol{u}_f$ (projection step);

(*d*) $\boldsymbol{u}_i := \boldsymbol{R}^*\boldsymbol{u}_f$ (adjoint problem, solve the adjoint equation backward in time from t_f to t_i.)

The renormalization step is used to ensure that the initial time norm $\|\boldsymbol{u}_i\|_i$ of the perturbation velocity at the initial time is always equal to 1. This avoids a rapid divergence of the norm (multiplied by about the biggest eigenvalue of $\boldsymbol{R}^*\boldsymbol{P}^*\boldsymbol{P}\boldsymbol{R}$ at each iteration). The operator $\boldsymbol{R}^*$ used in our simulations is a finite-difference approximation of the continuous adjoint to the linearized Navier–Stokes equation. After a minimum of four iterations the iterations were stopped when the ratio $\|\boldsymbol{u}_f\|_f / \|\boldsymbol{u}_i\|_i$, which was observed to increase monotonically from iteration to iteration, changed by less than 1 % in one iteration.

In the standard formulation of the generalized optimal perturbation problem the projection operator has to be of the form $\int u\,\delta(y-y_0)\,\mathrm{d}S$, where δ is the delta function. When the adjoint problem is to be solved backward in time with such an initial condition, the finite-difference approximation of the continuous adjoint operator will not be valid. To circumvent this difficulty, the Dirac delta function was approximated as a function p_δ centred at $y = y_0$:

$$p_\delta(y) = \begin{cases} f_\delta \exp\left(\dfrac{4\delta^2}{(y-y_0)^2 - \delta^2}\right) & \text{if } |y-y_0| < \delta/2, \\ 0 & \text{if } |y-y_0| \geqslant \delta/2, \end{cases} \tag{A 4}$$

where y_0 is the position of the projection layer, δ is the width of the projection function and f_δ is a renormalization coefficient to ensure that $\int_{y=-l}^{l} p_\delta(y)\mathrm{d}y = 1$.

The width δ of the projection function should be large enough for the finite-difference approximation to be good enough, but also small enough to ensure a good approximation of a Dirac delta function. A trade-off between these two requirements determines the grid size. A test of the optimization of a given case for different projection function widths is shown in figure 17. For the smallest width, only one point on the grid has a non-zero image of the projection. It turned out that even in this case the value of the optimal growth is close to the one obtained when there are more non-zero points with wider projection function. On the basis of this observation a one-grid-point projection was used for all the simulations shown in this paper. This choice gives the greatest numerical efficiency.

It is worth noting that calculating a generalized optimal perturbation using adjoint optimizations is more computationally expensive than a similar calculation of a standard optimal perturbation. This is because of the necessity to resolve or at least near-resolve the δ-function of $y - y_0$. As a result, the grid has to be sufficiently fine not only near the wall but also near the plane $y = y_0$.

The code was validated by reproducing the generalized optimal perturbation results of Chernyshenko & Baig (2005), which were obtained using a very different numerical method but for a non-oscillating wall only, and by reproducing the results of L. Burini & T. A. Zaki (personal communication, 2011) for optimal (but not generalized optimal) perturbations for a boundary layer on a spanwise-oscillating wall.

https://doi.org/10.1017/jfm.2013.165 Published online by Cambridge University Press

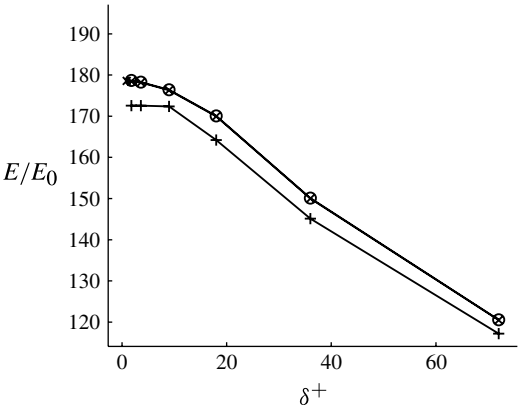


FIGURE 17. Influence of δ on the amplification factor. The number of grid points in the wall-normal direction is $ny = 129$ (+), $ny = 513$ (∘), and $ny = 1025$ (×).

REFERENCES

ADRIAN, R. J. 2007 Hairpin vortex organization in wall turbulence. *Phys. Fluids* **19** (4), 041301.

BAMIEH, B. & DAHLEH, M. 2001 Energy amplification in channel flows with stochastic excitation. *Phys. Fluids* **13** (11), 3258–3269.

BARON, A. & QUADRIO, M. 1996 Turbulent drag reduction by spanwise wall oscillations. *Appl. Sci. Res.* **55**, 311–326.

BATCHELOR, G. K. & PROUDMAN, I. 1954 The effect of rapid distortion of a fluid in turbulent motion. *Q. J. Mech. Appl. Maths* **VII**, 83–103.

BIAU, D. & BOTTARO, A. 2009 An optimal path to transition in a duct. *Phil. Trans. R. Soc. Lond.* **367** (1888), 529–544.

BRADSHAW, P. & PONTIKOS, N. S. 1985 Measurements in the turbulent boundary layer on an infinite swept wing. *J. Fluid Mech.* **159**, 105–130.

BUTLER, K. M. & FARRELL, B. F. 1993 Optimal perturbations and streak spacing in wall-bounded turbulent shear flow. *Phys. Fluids* A **5** (3), 774–777.

CAMBON, C. & SCOTT, J. F. 1999 Linear and nonlinear models of anisotropic turbulence. *Annu. Rev. Fluid Mech.* **31**, 1–53.

CARPENTER, P. W., KUDAR, K. L., ALI, R., SEN, P. K. & DAVIES, C. 2007 A deterministic model for the sublayer streaks in turbulent boundary layers for application to flow control. *Phil. Trans. R. Soc. Lond.* A **365**, 2419–2441.

CHERNYSHENKO, S. I. & BAIG, M. F. 2005 The mechanism of streak formation in near-wall turbulence. *J. Fluid Mech.* **544**, 99–131.

CHERNYSHENKO, S. I., MARUSIC, I. & MATHIS, R. 2012 Quasi-steady description of modulation effects in wall turbulence. arXiv/1203.3714.

CHOI, K.-S. 2002 Near-wall structure of turbulent boundary layer with spanwise-wall oscillation. *Phys. Fluids* **14** (7), 2530–2542.

CHOI, K.-S. & CLAYTON, B. R. 2001 The mechanism of turbulent drag reduction with wall oscillation. *Intl J. Heat Fluid Flow* **22** (1), 1–9.

CHOI, K.-S., CLAYTON, B. R. & DEBISSCHOP, J.-R. 1998 Turbulent boundary-layer control by means of spanwise-wall oscillation. *AIAA J.* **36**, 1157–1163.

COSSU, C., PUJALS, G. & DEPARDON, S. 2009 Optimal transient growth and very large-scale structures in turbulent boundary layers. *J. Fluid Mech.* **619**, 79–94.

CVITANOVIĆ, P. & GIBSON, J. F. 2010 Geometry of the turbulence in wall-bounded shear flows: periodic orbits. *Phys. Scr.* **2010** (T142), 014007.

DEL ÁLAMO, J. C. & JIMÉNEZ, J. 2006 Linear energy amplification in turbulent channels. *J. Fluid Mech.* **559**, 205–213.

https://doi.org/10.1017/jfm.2013.165 Published online by Cambridge University Press

DUGUET, Y., PRINGLE, C. C. T & KERSWELL, R. R 2008 Relative periodic orbits in transitional pipe flow. *Phys. Fluids* **20** (11), 114102.

DUQUE-DAZA, C. A., BAIG, M. F., LOCKERBY, D. A., CHERNYSHENKO, S. I. & DAVIES, C. 2012 Modelling turbulent skin-friction control using linearized Navier–Stokes equations. *J. Fluid Mech.* **702**, 403–414.

FAISST, H. & ECKHARDT, B. 2003 Traveling waves in pipe flow. *Phys. Rev. Lett.* **91** (22), 224502.

FARRELL, B. F. & IOANNOU, P. J. 1993*a* Optimal excitation of three-dimensional perturbations in viscous constant shear flow. *Phys. Fluids* A **5**, 1390–1400.

FARRELL, B. F. & IOANNOU, P. J. 1993*b* Stochastic forcing of the linearized Navier–Stokes equations. *Phys. Fluids* A **5** (11), 2600–2609.

FARRELL, B. F. & MOORE, A. M. 1991 An adjoint method to obtain most rapidly growing perturbations in oceanic flows. *J. Phys. Oceanogr.* **22**, 338–349.

GASTER, M., KIT, E. & WYGNANSKI, I. 1985 Large-scale structures in a forced turbulent mixing layer. *J. Fluid Mech.* **150**, 23–39.

HAMILTON, J. M., KIM, J. & WALEFFE, F. 1995 Regeneration mechanisms of near-wall turbulence structures. *J. Fluid Mech.* **287**, 317–348.

HILL, D. C. 1995 Adjoint systems and their role in the receptivity problem for boundary layers. *J. Fluid Mech.* **292**, 183–204.

HUNT, J. C. R. 1973 A theory of turbulent flow round two-dimensional bluff bodies. *J. Fluid Mech.* **61**, 625–706.

HUNT, J. & KEVLAHAN, N. 1993 Rapid distortion theory and the structure of turbulence. In *New Approaches and Concepts in Turbulence* (ed. T. Dracos & A. Tsinober). pp. 285–316. Birkhauser.

HUTCHINS, N., MONTY, J. P., GANAPATHISUBRAMANI, B., NG, H. C. H. & MARUSIC, I. 2011 Three-dimensional conditional structure of a high-Reynolds-number turbulent boundary layer. *J. Fluid Mech.* **673**, 255–285.

HWANG, Y. & COSSU, C. 2010 Linear non-normal energy amplification of harmonic and stochastic forcing in the turbulent channel flow. *J. Fluid Mech.* **664**, 51–73.

JIMÉNEZ, J. & MOIN, P. 1991 The minimal flow unit in near-wall turbulence. *J. Fluid Mech.* **225**, 213–240.

JIMÉNEZ, J. & PINELLI, A. 1999 The autonomous cycle of near-wall turbulence. *J. Fluid Mech.* **389**, 335–359.

JOVANOVIĆ, M. & BAMIEH, B. 2001 Modelling flow statistics using the linearized Navier–Stokes equations. In *Proceedings of the 40th IEEE Conference on Decision and Control*, vol. 5, pp. 4944–4949.

JOVANOVIĆ, M. R. & BAMIEH, B. 2005 Componentwise energy amplification in channel flows. *J. Fluid Mech.* **534**, 145–183.

JOVANOVIĆ, M. & GEORGIOU, T. 2010 Reproducing second-order statistics of turbulent flows using linearized Navier–Stokes equations with forcing. In *APS Division of Fluid Dynamics Meeting 2010, Abstracts*, p. C10.

JUNG, W. J., MANGIAVACCHI, N. & AKHAVAN, R. 1992 Suppression of turbulence in wall-bounded flows by high-frequency spanwise oscillations. *Phys. Fluids* A **4** (8), 1605–1607.

KARNIADAKIS, G. E. & CHOI, K.-S. 2003 Mechanisms on transverse motions in turbulent wall flows. *Annu. Rev. Fluid Mech.* **35**, 45–62.

KAWAHARA, G. 2009 Ivited review: theoretical interpretation of coherent structures in near-wall turbulence. *Fluid Dyn. Res.* **41** (6), 064001.

KAWAHARA, G. & KIDA, S. 2001 Periodic motion embedded in plane Couette turbulence: regeneration cycle and burst. *J. Fluid Mech.* **449**, 291–300.

KERWELL, R. R. & TUTTY, O. R. 2007 Recurrence of travelling waves in transitional pipe flow. *J. Fluid Mech.* **584**, 69–102.

KIM, J. & LIM, J. 2000 A linear process in wall-bounded turbulent shear flows. *Phys. Fluids* **12** (8), 1885–1888.

https://doi.org/10.1017/jfm.2013.165 Published online by Cambridge University Press

KIM, J., MOIN, P. & MOSER, R. 1987 Turbulence statistics in fully developed channel flow at low Reynolds number. *J. Fluid Mech.* **177**, 133–166.

KLINE, S. J., REYNOLDS, W. C., SCHRAUB, F. A. & RUNSTADLER, P. W. 1967 The structure of turbulent boundary layers. *J. Fluid Mech.* **30** (4), 741–773.

LAADHARI, F., SKANDAJI, L. & MOREL, R. 1994 Turbulence reduction in a boundary layer by a local spanwise oscillating surface. *Phys. Fluids* **6** (10), 3218–3220.

LAIZET, S. & LAMBALLAIS, E. 2009 High-order compact schemes for incompressible flows: a simple and efficient method with quasi-spectral accuracy. *J. Comput. Phys.* **228** (16), 5989–6015.

LANDAHL, M. T. 1975 Wave breakdown and turbulence. *SIAM J. Appl. Maths* **28**, 735–756.

LEE, M. J., KIM, J. & MOIN, P. 1990 Structure of turbulence at high shear rate. *J. Fluid Mech.* **216**, 561–583.

LEVICH, R. A., HANDLERAND, E. & SIROVICH, L. 1993 Drag reduction in turbulent channel flow by phase randomization. *Phys. Fluids* A **5** (6), 686–694.

LOCKERBY, D., CARPENTER, P. & DAVIES, C. 2005 Control of sublayer streaks using microjet actuators. *AIAA J.* **43**, 1878–1886.

LUCHINI, P. 2000 Reynolds-number-independent instability of the boundary layer over a flat surface: optimal perturbations. *J. Fluid Mech.* **404**, 289–309.

MCKEON, B. J. & SHARMA, A. S. 2010 A critical-layer framework for turbulent pipe flow. *J. Fluid Mech.* **658**, 336–382.

MOARREF, R. & JOVANOVIĆ, M. R. 2012 Model-based design of transverse wall oscillations for turbulent drag reduction. *J. Fluid Mech.* **707**, 205–240.

MOIN, P., SHIH, T.-H., DRIVER, D. & MANSOUR, N. N. 1990 Direct numerical simulation of a three-dimensional turbulent boundary layer. *Phys. Fluids* A **2**, 1846–1853.

NAZARENKO, S., KEVLAHAN, N. K.-R. & DUBRULLE, B. 2000 Nonlinear RDT theory of near-wall turbulence. *Physica* D **139** (1–2), 158–176.

PANTON, R. L. 1997 Self-sustaining mechanisms of wall turbulence. In *Advances in Fluid Mechanics*, vol. 15. Computational Mechanics Publications.

PUJALS, G., GARCÍA-VILLALBA, M., COSSU, C. & DEPARDON, S. 2009 A note on optimal transient growth in turbulent channel flows. *Phys. Fluids* **21** (1), 015109.

QUADRIO, M. 2011 Drag reduction in turbulent boundary layers by in-plane wall motion. *Phil. Trans. R. Soc. Lond.* A **369** (1940), 1428–1442.

QUADRIO, M. & RICCO, P. 2004 Critical assessment of turbulent drag reduction through spanwise wall oscillations. *J. Fluid Mech.* **521**, 251–271.

QUADRIO, M., RICCO, P. & VIOTTI, C. 2009 Streamwise-travelling waves of spanwise wall velocity for turbulent drag reduction. *J. Fluid Mech.* **627**, 161–178.

REYNOLDS, W. C. & HUSSAIN, A. K. M. F. 1972 The mechanics of an organized wave in turbulent shear flow. Part 3. Theoretical models and comparisons with experiments. *J. Fluid Mech.* **54**, 263–288.

REYNOLDS, W. C. & TIEDERMAN, W. G. 1967 Stability of turbulent channel flow, with application to Malkus's theory. *J. Fluid Mech.* **27** (2), 253–272.

RICCO, P. 2004 Modification of near-wall turbulence due to spanwise wall oscillations. *J. Turbul.* **5**, N24.

RICCO, P. & QUADRIO, M. 2008 Wall-oscillation conditions for drag reduction in turbulent channel flow. *Intl J. Heat Fluid Flow* **29** (4), 891–902.

ROBINSON, S. K 1991 Coherent motions in the turbulent boundary layer. *Annu. Rev. Fluid Mech.* **23**, 601–639.

SCHMID, P. J. 2007 Nonmodal stability theory. *Annu. Rev. Fluid Mech.* **39**, 129–162.

SCHOPPA, W. & HUSSAIN, F. 2002 Coherent structure generation in near-wall turbulence. *J. Fluid Mech.* **453**, 57–108.

SEN, P. K. & VEERAVALLI, S. V. 1998 On the behaviour of organized disturbances in a turbulent boundary layer. *Sādhāna* **23**, 167–193.

SEN, P. K. & VEERAVALLI, S. V. 2000 Hydrodynamic stability theory and wall turbulence. *Curr. Sci. India* **79** (6), 840–848.

https://doi.org/10.1017/jfm.2013.165 Published online by Cambridge University Press

SEN, P. K., VEERAVALLI, S. V., CARPENTER, P. W., JOSHI, G. & JOSAN, P. S. 2007 Organized structures in wall turbulence as deduced from stability theory-based methods. *Sādhāna* **32**, 51–64.

SMITH, C. R. & METZLER, S. P. 1983 The characteristics of low-speed streaks in the near-wall region of a turbulent boundary layer. *J. Fluid Mech.* **129**, 27–54.

TOUBER, E. & LESCHZINER, M. 2012 Near-wall streak modifications by spanwise oscillatory wall motions and relationship to friction-drag reduction. *J. Fluid Mech.* **693**, 150–200.

VISWANATH, D. 2007 Recurrent motions within plane couette turbulence. *J. Fluid Mech.* **580**, 339–358.

WALEFFE, F. 1998 Three-dimensional coherent states in plane shear flows. *Phys. Rev. Lett.* **81**, 4140–4143.

WALEFFE, F. 2001 Exact coherent structures in channel flow. *J. Fluid Mech.* **435**, 93–102.

https://doi.org/10.1017/jfm.2013.165 Published online by Cambridge University Press